Title
Particle Finite Element Modeling of Nanoparticle-Photopolymer Composites for Additive Manufacturing

Author
Hays, Shanna Angelique

Publication Date
2019

Peer reviewed|Thesis/dissertation

Particle Finite Element Modeling of Nanoparticle-Photopolymer Composites for Additive Manufacturing

by

Shanna Angelique Hays

A dissertation submitted in partial satisfaction of the

requirements for the degree of

Doctor of Philosophy

in

Engineering - Mechanical Engineering

in the

Graduate Division

of the

University of California, Berkeley

Committee in charge:

Professor Tarek Zohdi, Chair
Professor Lisa Pruitt
Professor James Sethian

Summer 2019

Particle Finite Element Modeling of Nanoparticle-Photopolymer Composites for Additive Manufacturing

Abstract

Particle Finite Element Modeling of Nanoparticle-Photopolymer Composites for Additive Manufacturing

by

Shanna Angelique Hays

Doctor of Philosophy in Engineering - Mechanical Engineering

University of California, Berkeley

Professor Tarek Zohdi, Chair

Additive manufacturing (AM) has had continued and growing appeal in academia and industry due to its ability to create customizable designs containing complex geometries and internal structures, reduce time to move from concept to final product for low volume production runs, and utilize a wide range of materials. One specific area of interest is the inclusion of additives into AM materials creating opportunities to produce parts with tailored material properties with specific functionality. For example, the addition of nanoparticles, such as carbon nanotubes and semiconductor nanocrystals, into polymers have lead to the creation of customizable micrometer sized strain gauges and light-emitting devices [18, 30]. While the additives provide many benefits, they lead to undesired changes to the material response during manufacturing that require modifying the process parameters to maintain print quality.

The focus of this work is the development of a computational modeling tool that captures the changes in the material response of nanoparticle-photopolymer composites for process parameter optimization in inkjet printing. This is achieved by introducing the photopolymerization process to the thermo-mechanical model within the particle finite element method (PFEM) framework. The simulation portion of this work is then broken into two parts. First, the effects of additives are investigated in two simple model problems, the deposition of a single droplet and stereolithography type process, designed to limit the influence of process parameters. Second, the effects of process parameters on a nanoparticle-photopolymer composite are studied to develop an objective function to characterize the results of the simulations.

To my husband, Sean Hays,
for helping me make my dreams a reality.

Contents

List of Figures

List of Tables

Acknowledgments

First I would like to express my deepest appreciation to my advisor Prof. Tarek Zohdi for his support and mentorship through my PhD studies. I appreciate the valuable insight you provided and the freedoms you afforded to grow and develop my own interests.

I would like to express my sincere thanks to my committee members Prof. Lisa Pruitt and Prof. James Sethian for the advise and support through my coursework and dissertation. I would like to thank Prof. Ibrahim Guven for his encouragement during my undergraduate and early graduate studies.

I would like to thank my friends and lab mates in the Computational Manufacturing and Materials Research Lab (CMMRL) for always providing an inclusive and welcoming space to work and socialize. I am thankful for my closest friends Amanda Veitch and Shannon Emerzian who helped keep me sain during the toughest times.

Finally, I would like to thank my parents, Rich and Gwen, and sisters, Dani and Stephanie, for their never ending love and support in everything I do. It is because of you I have the confidence to push myself to explore the unknown.

This work was supported in part by the Army High Performance Computing Research Center and Army Research Lab.

Chapter 1

Introduction

1.1 Motivation

Additive manufacturing (AM), also known as 3D Printing, is a process in which a part is produced by adding material in a repetative deposition or solidification process, often in a layer upon layer manner. While many technologies exist, the most common are direct write systems, such as fused deposition modeling (FDM), in which a polymer is extruded onto a build platform, powder bed fusion in which a laser sinters powdered material, stereolithography (SLA) in which a laser cures a vat of photopolymer, and material jetting printing (MJP), or inkjet printing (IJP), in which an ink is jetted onto a build surface and immediately solidified. Interest in AM continues in academia and industry for the potential applications in a wide range of fields, including sports, medical, pharmaceutical, and aerospace. The reason AM has such wide appeal is the ability to create customizable designs containing complex geometries and internal structures, reduce time to move from concept to final product for low volume production runs, and utilize a wide range of materials (i.e. metals, ceramics, and polymers).

While the technology has many uses as is, the introduction of additives into AM materials creates opportunities to produce parts with tailored material properties with specific functionality on the micrometer scale. For example, the addition of nanoparticles, e.g. carbon nanotubes, semiconductor nanocrystals, into polymer results in parts with tailored material response(s), e.g. electrical, thermal, or mechanical properties. To make the most of the new composite materials, we must improve our understanding of how these materials behave during the AM process and over come the challenges that additives introduce.

The work presented here is driven by the problem of understanding the behavior of nanoparicle-polymeric composites in AM to optimize process parameters and assist in continued development of new materials. In the remainder of this chapter, a brief overview of applications of additives in AM is provided in Section 1.2. A review of the inkjet printing process and current challenges is provided in Section 1.3. Finally, an outline for the remaining chapters are provided in Section 1.4.

1.2 Additives in Additive Manufacturing

One subset of applications for additives in AM is in printed electronics. Carbon nanotubes have been combined with polymers to produce macro or microdevices that have improved mechanical strength and electrical conductivity [19], create electromagnetic interference (EMI) shielding [7], and microscale mechanical components [32]. Strain gauges capable of being directly printed into a device has been demonstrated by adding silver precursores ($AgSbF_6$) and titanium (TiO_2) to a photopolymer [6]. The inclusion of semiconductor nanoparticles results in devices capable of producing optical sensors [17] and light-emitting devices (LEDs) [50]. A review of further applications can be found in [18, 30].

For printed electronics, the common manufacturing techniques employed are SLA, direct write systems, such as FDM, and inkjet printing. SLA has the most limited applications to printed electronics as the process requires a laser to selectively cure the surface of a vat of photopolymer. Once the layer is complete the part moves further into the vat and the process repeats. By the nature of SLA, only a single material can be utilized limiting the application to components with a single functionality [33]. Direct write systems are able to avoid single material limitations by having multiple nozzles that extrude different materials. The largest challenges posed by direct write systems comes from material being deposited as individual lines. Firstly, to achieve a resolution on the micrometer scale, the nozzle must become smaller decreasing the deposotion rate resulting in a slow build process. Secondly, adjacent deposited lines do not achieve perfect adhesion limiting the applications to path independent designs, Figure 1.1. The final method, inkjet printing, avoids the problems of the previous two methods as it can print with multiple materials, achieve micrometer scale resolution, and the timing of solidification improves bonding between deposited material reducing anisotropic properties. For flexible electronics with large surface areas and small build heights that incorporate multiple materials, the inkjet printing process posses the most advantages. Details of the process and challenges associated with inkjet printing are detailed in the next section.

1.3 Process Overview

Inkjet printing with photopolymers originates with the inkjet printer. In the 1980's a three-dimensional printing method was demonstrated through the deposition of "particles of material". The first commercially successful technology printed a wax heated to a liquid state and cooled upon deposition. Commercial machines continued to utilize wax through the 1990's. During this time research was underway to develop photocurable resins similar to those found in SLA for inkjet printing. Machines that successfully deposited liquid drops of photocurable resins were introduced by the early 2000's [22].

The the inkjet printing process utilizes the same print heads developed for standard inkjet printers [46]. A series of print heads containing hundreds of nozzles scan across the build platform depositing a single layer of material. Each print head is heated to reduce

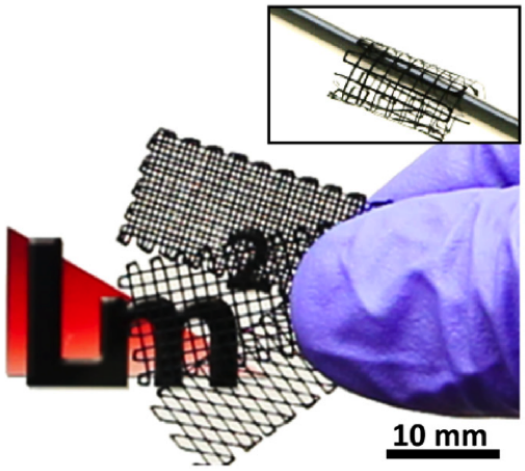

Figure 1.1: FDM printed electromagnetic interference shielding composed of a multi-walled carbon nanotubes and polylactic acid (PLA) composite [7].

the viscosity of the resin for printing; once the resin leaves the nozzle it begins to cool to prevent the droplet from speading too thin upon impact. Following the print heads an ultraviolet light scans across causing a chemical reaction to occur within the resin resulting in solidification through polymerization. The print heads then make a return pass depositing more material on the partially cured material followed by the light. Since prints may require support material a secondary material, such as a wax, is also deposited from some of the nozzles. The process of depositing material then curing is repeated until a fully formed part is produced, Figure 1.2.

Many challenges exist during the printing process that must be addressed to produce high resolution printed parts. First, the formation of the droplet poses a challenge as small changes to the chemical composition or the introduction of particles changes the behavior of shape and volume of the droplet produced. Second, the droplet deposition, specifically the flight path and impact behavior, pose a challenge as new layers of droplets must land precisely on the previous layer and combine to produce smooth, stable print lines. The third challenge is the timing of droplet solidification. A liquid droplet is ejected from the nozzle and must impact and form a solid part through a phase change; the timing of the phase change can impact the final part geometry and quality. The following sections discuss each of these challenges in greater detail and how they are currently addressed.

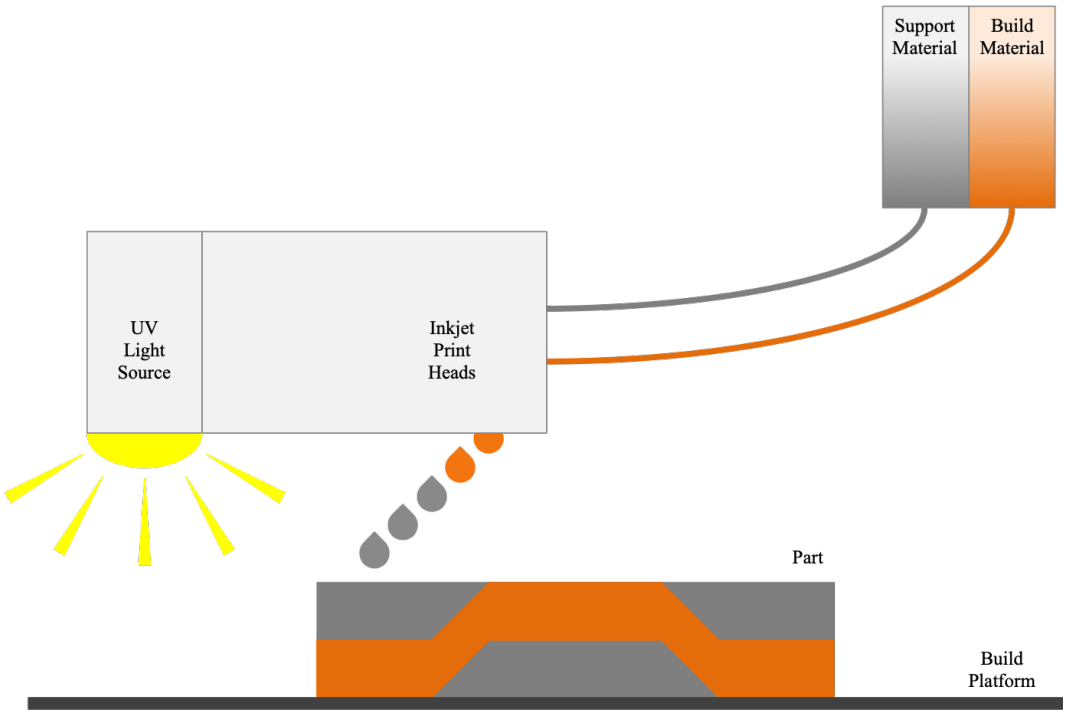

Figure 1.2: Overview of the inkjet printing process.

1.3.1 Droplet Formation

Changes in the chemical composition or the inclusion of particle additives results in a change in the droplet formation process due to the change in material properties. To understand why the change in behavior occurs, we must first understand how droplets are formed. The primary method for dorplet formation is the drop-on-demand technology where a controlled pressure pulse is induced within the liquid filled nozzle resulting in fluid being ejected through the nozzle opening. To produce a rapid pressure change, the prominent actuator for thermally sensitive materials are piezoelectric in which a film of material is rapidly expanded physically displacing the fluid. The characteristics of the pressure pulse are controlled by the voltage into the piezoelectric and the dwell time; the voltage controls the displacement into the fluid while the dwell time controls how long the displacement is maintained.

The ideal values for the voltage and dwell time are dependent upon the fluid viscosity and surface tension. If the viscosity and surface tension become too large, the pressure pulse does not provide enough energy to produce a droplet. On the other hand, if the values are too small, the fluid may be too sensitive to motion and produce a droplet when none is desired. Analytical models have been developed to determine the range of material properties in which the material can feasibly be printed [12, 52]. Derby [11] combined the various models into a plot of the Weber number versus Reynolds number to demonstrate the range of values that produce droplets, Figure 1.3.

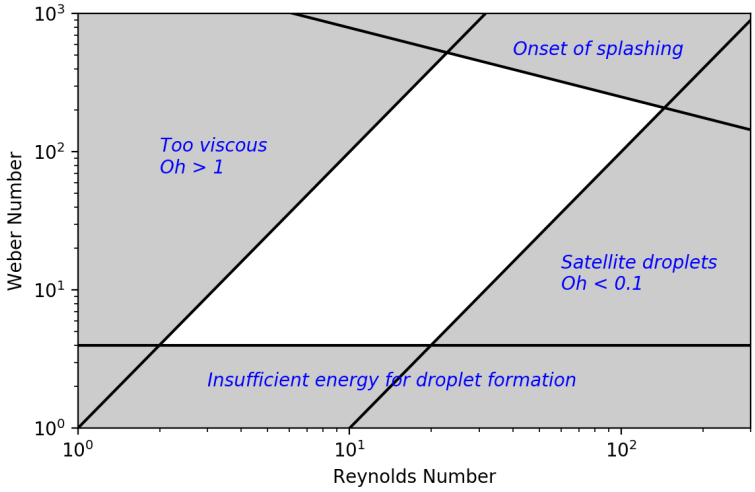

Figure 1.3: Range of printable materials based upon Weber and Reynolds number, adapted from Derby [11].

The introduction of additives complicates these dependencies as the material may become shear thinning thus allowing for a higher design viscosity but the surface tension may also increase resulting in a material that is no longer printable [38]. Derby and Reis [10] demonstrated that the analytical range previously described can be applied to particle laden fluids in determining the printability of the fluid. Elliot et al. [16, 17] experimentally demonstrated that when quantum dots are introduced to a photopolymer in an inkjet printing head, the material is printable but there is a change in the droplet characteristics, i.e. the length of the tail, the formation of satillite droplets, and the volume of the droplets. While their findings demonstrate that inkjet printing with additives is possible, it does not inform how the process parameters might need to be changed to obtain optimal performance of the new materials.

One method to determine optimal parameters is to perform experiments in which process parameters are varied until optimal designs are obtained. A challenge is that the inkjet printing process operates with tiny droplets, 4 to 65 picoliters, ejected at high velocity, 4 to 9 m/s, and high frequency, 0.25 to 20 kHz, making image capture a challenge [11, 31]. To avoid these challenges, computational models supplement the experimental work in the early stages reducing the need to maintain experimental set ups for long periods of time. There has been success in the modeling of viscoelastic fluids in inkjet printing with level set projection method [57, 58, 59]. The primary limitation for these models is that they do not address variations in behavior due to the presence of additives.

While currently beyond the scope of this work, computational models allow for the determination of optimal process parameters without requiring extensive experimentation and prior knowledge of the technology.

1.3.2 Droplet Deposition

Once the ability to form a single stable droplet is overcome, the next challenge is the deposition of multiple droplets in quick succession that produce a smooth and stable print line. This can be broken into two parts; control of the droplets during flight to ensure even spacing upon impact and determining the spacing of material to produce the desired print lines.

During the droplet flight, one of the most important factors is the droplet ejection velocity. If all of the droplets are released at the same velocity and the print head is moving at a constant velocity, a uniform spacing between droplets can be maintained. In practicality, droplets are ejected at variable velocities which can result in droplets merging during flight. The variablility in velocities comes from the reflection of pressure waves mixing with the current pressure pulse, by adding a quenching pulse, in which the piezoelectric actuator deforms out of the material, a pocket that can arrest the pressure pulse is formed [31]. While the issue of uniform ejection velocities remains an open topic of research it is beyond the scope of this work and thus the flight behavior of droplets is not considered.

While the study of voltage profiles is beyond the scope of this work, an important byproduct of introducing a quenching pulse is that the time to form a droplet is increased. This increase in times directly impacts the frequency in which droplets can be released which in turn limits the control parameters for producing smooth and stable print lines.

In addition to the timing between droplet an important consideration is the spacing between droplets. If droplets are spaced too far apart individuals droplets or lines in which droplets could not fully merge can form while droplets spaced too close together can result in an unstable line that has buldges with high volumes of material [51], Figure 1.4. Analytical models have been developed to determine the optimal spacing between droplets to produce stable print lines [51, 54] but the work found that their methods showed poor agreement with experimental results for some material types. Computational models have the potential to overcome the limitations of the analytical models since no assumptions are made about the final shape of the deposited material and the physics are able to drive the final results.

Since the focus of this work is on the introduction of additives into photopolymers for AM, the primary challenge focused on is understanding the stability print lines. This is broken into two parts; how do additives impact the deposition behavior of the photopolymer and given a desired volume fraction of material, develop a method for characterizing the quality of the print lines to determine optimal process parameters. The quality of the print lines is determined by characterizing the print profile through measurable values and determining the limiations on the values that produce smooth and stable surfaces.

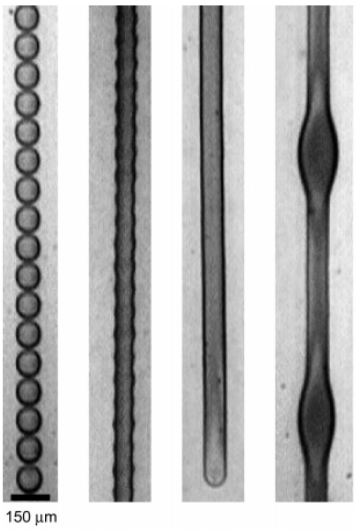

Figure 1.4: Different print line structures observed by Soltman and Subramanian [51]. From left to right: individual drops, a scalloped line, a uniform line, and a bulging line.

1.3.3 Droplet Solidification

Once the position of a droplet is determined, the next challenge is to address the solidification behavior. For the photopolymerization inkjet printing process, there are two solidification steps. First, the material is heated in the nozzle to reduce the viscosity and allow for droplet formation. Once the droplet is ejected from the nozzle it begins to cool allowing for some of the droplet shape to be maintained while also allowing for complete merger of subsequent droplets. Next, the UV light passes over the material and chemical solidification begins. The chemical solidification turns the fluid resin into a solid polymer.

The timing of solidification is key to producing a uniform solid part that does not warp or curl. Thermal solidification governs the behavior of the droplet during the deposition process. If thermal solidification occur too early in the process, the droplets may not spread enough resulting in nonuniform material distribution. The chemical solidification governs the quality of the final component. During the photopolymerization process as the degree the material has polymerized, or cured, increases the material begins to shrink. If the difference in the degree of cure between two layers is too large, the top layer will shrink after the bottom layer resulting in compressive stresses at the top of the bottom layer and tensile stresses at the bottom of the top layer. These internal stresses lead to curling or warping in parts with at least two dimension having a large aspect ratio.

The introduction of additives complicates the solidification behavior, especially during the chemical solidification, since they may either absorb or reflect the incident UV light reducing the degree of cure below the particles. Elliott et al. [16] experimentally demonstrated the necessity to study how additives adversely affect the cure depth of photopolymers with quantum dots, Figure 1.5.

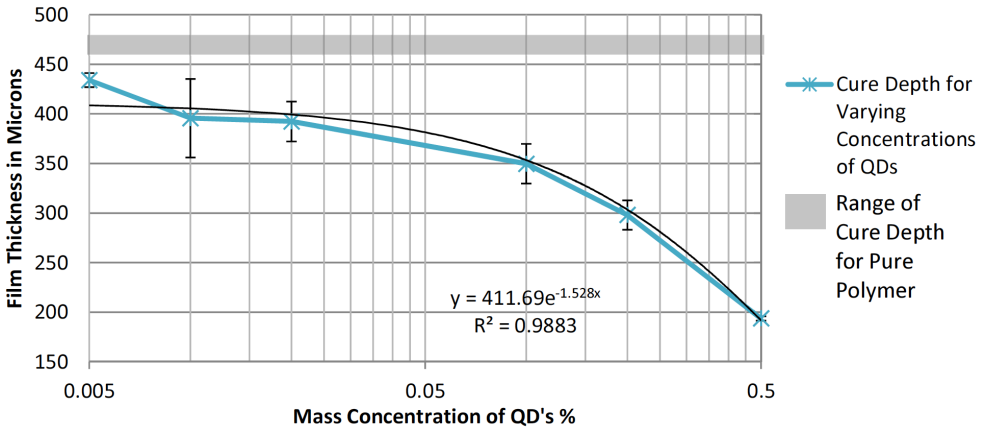

Figure 1.5: Maximum cure depth for photopolymer with quantum dots after applying a 52mJ/cm^2 energy dose at a wavelength of 365 nm [16].

Aside from the material itself, there are various factors controlling the solidification behavior. During thermal solidification, primary control factors are the temperature of the nozzle, build surface, and environment. The temperature of the nozzle controls the material viscosity during the early stages of deposition since higher temperatures results in lower viscosities. The later stages of thermal solification are controlled by the environment and build surface since they control how quickly the material cools.

The primary control factors during chemical solidification are the irradience of the light source and the length of time the material is exposed to the light source. As the irradience is increased, the photoinitiators absorb more energy allowing for greater conversion rates of monomer into polymer chains. Increasing the length of exposure has a similar effect in that the longer the material is exposed, the more time the polymer chains have to propagate.

Since SLA has been a commercially available technology since the 1980's, many computational and mathematical models have been developed that capture the thermo-chemical response during SLA printing [3, 45, 48, 49]. Much of the work has been on path optimization or the development of material characterization with no consideration for the motion of the material as a liquid, gel, or solid. If additives are included, they are only done so through modifying the effective absorptivity of the material.

To address changes resulting from introducing additives, this problem is divided into two parts. The first is to understand how additives change the curing behavior of the material and the second is to look at how we can determine process parameters that provide the best curing behavior.

1.4 Outline of Work

The next chapters first develop the computational method then address two of the primary challenges in the inkjet printing process with additive-photopolymers composities. Chapter 2 introduces the particle finite element method (PFEM) used to model the impact of the droplet and stability of print lines. Chapter 3 expands upon the PFEM to introduce a curing model to simulate the curing phase of the printing process. Chapters 4 and 5 address the specific focus of this work, to understand the effects of additives given fixed process parameters on the thermo-mechano-chemical response and the development of an objective function capable of characterizing how well the process parameters performed, respectively. Chapter 6 provides closing remarks concerning what was achieved and future extension of this work.

Chapter 2

Particle Finite Element Method

2.1 Method Overview

The particle finite element method (PFEM) is selected as the analysis tool due to the ability to include multiphysics into a single solution scheme while permitting large deformations, separation, and combination of material surfaces, and fluid-solid interactions [26, 41, 42, 43]. These capabilities come from coupling Lagrangian particles with the integral formulation of the finite element method (FEM). The primary benefit of implementing a Lagrangian formulation is that the convective terms are eliminated.

In the PFEM, fluid and solid domains are discretized into an arbitary number of particles. All variables of the fluid and solid particles are known, such as temperature, velocity, and position, at the current configuration, time t. To determine the variables at the new configuration, time $t + \Delta t$, the FEM is utilized to calculate the interaction forces between neighboring particles where the particles serve as the nodes of the mesh. Once the forces are calculated the mesh is disregarded and particles are able to move freely according to their velocity field and physical properties. Figure 2.1 visually respresents the PFEM process.

The steps for a typical solution generated utilizing the PFEM is as follows:

1. Start with the particles in the current configuration, time t.
2. Identify the boundary of the domain using the α-shape method [13, 44], details discussed in Section 2.4. This boundary represents the free surface of the entire material. The proximity of different particles results in the separation and merging of domains.
3. Mesh the domain within all boundaries using particles as the nodes of the mesh. Meshing is achieved through Delaunay triangulation, details discussed in Section 2.4.
4. Solve the Lagrangian form of the continuum equations using the FEM to compute variables, such as velocities, pressures, and temperatures, for the new configuration, time $t + \Delta t$.
5. Move the particles to their new position.

6. Return to Step 1 updating new values to current configuration and repeating the process for the next time step, stopping when desired stop time, t_f, is reached.

In the remainder of this chapter, the material constitutive equation is discussed in Section 2.2 and the govering equations for the thermo-mechanical model are covered in Section 2.3. The boundary identification and meshing are covered in Section 2.4. To solve using the FEM, the discretization of the governing equations is covered in 2.5. Finally, section 2.6 provides a detailed discussion of the solution scheme.

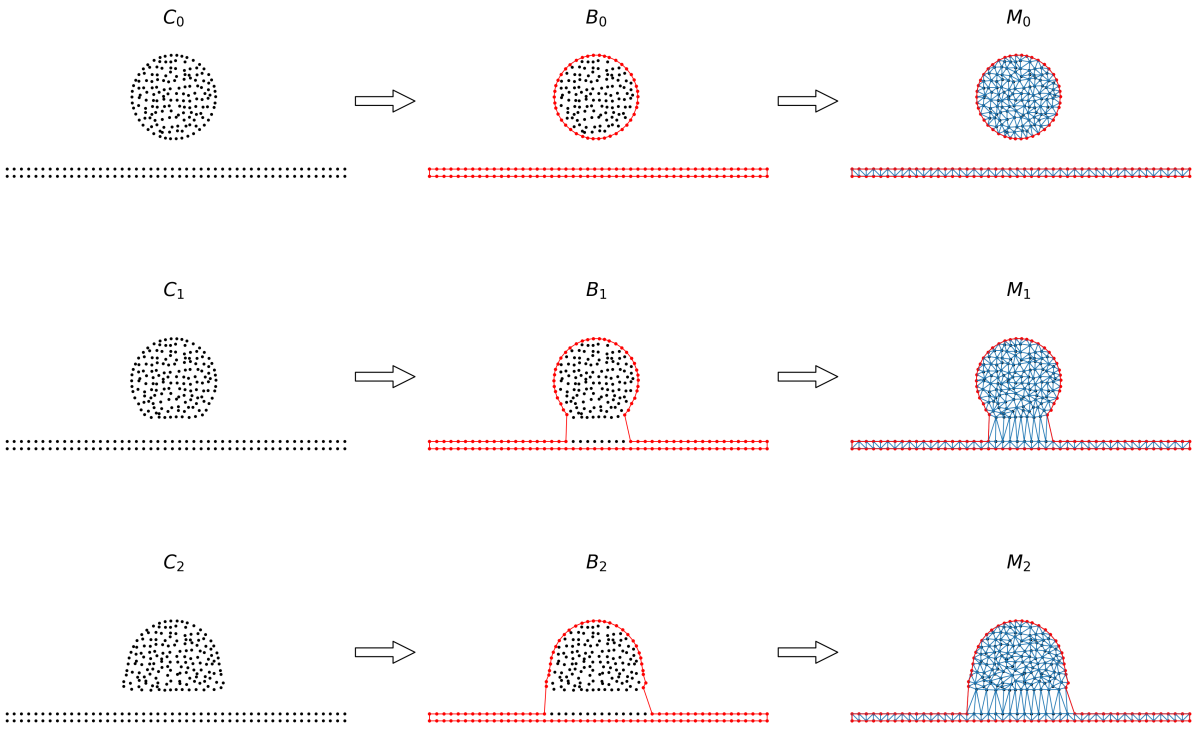

Figure 2.1: The PFEM process begins with the point cloud, C_0. Using the α-shape function all boundaries defining the point cloud are identified, B_0, and then the interior of each boundary are meshed using Delaunay triangulation, M_0. After determining the new velocity for each particle using the finite element method, the particles are moved to the next location at the next time step forming a new point cloud, C_1. The process is then repeated until desired end time. [43]

2.2 Polymer Constitutive Equation

Photopolymers after cure are cross-linked polymers so typically have a rubber type response but prior to polymerization, the resin is composed of monomers and oligomers which have

a viscous fluid rather than a viscoelastic solid response. For fluid systems the simplest of constitutive equations is the linear viscous fluid given by

$$\mathbf{T} = -p\mathbf{I} + 2\mu\mathbf{D} \tag{2.1}$$

where p is the hydrostatic pressure, $\mathbf{I}$ is the identity tensor, μ is viscosity, and $\mathbf{D}$ is the rate of deformation tensor which can be written alternatively as $\mathbf{D} = \frac{1}{2}((\nabla\mathbf{v}) + (\nabla\mathbf{v})^T) = (\nabla\mathbf{v})^s$.

Non-Newtonian effects are accounted for by defining the viscosity as a function of strain rate, $\mathbf{D}$, temperature, θ, degree of cure, C, and properties of additives, such as the volume fraction of additives Φ_a [40]. Ideally, the viscosity function would contain all of these dependencies, but in practice only a subset are used when fitting to experimental data. Based upon the set of experimental data available in the literature, only the dependencies upon temperature and volume fraction of additives are used in this work. To allow for a simple viscosity model, each of the non-Newtonian effects are considered independent and introduced as separate functions

$$\mu(\theta, \Phi_a) = f(\Phi_a)\, \mu(\theta). \tag{2.2}$$

First consider the temperature dependence; as the temperature increases, the viscosity decreases. Since the resin is comprised of relatively small oligomers and monomers the simplest of equation for temperature dependence is modeled with the Arrhenius shift, given as

$$\frac{\mu}{\mu_0} = \exp\left[\frac{E_\theta}{R\theta}\right] \tag{2.3}$$

where μ_0 is the a known viscosity at the reference temperature, E_θ is the activation energy of the material, and R is the universal gas constant.

The introduction of additives into a polymer increases the viscosity [40]. While the extent of the increase depends upon various features of the additives, such as volume fraction, shape, average size, and size distribution, and the interaction between additives and both the polymer matrix and other additives [36], most models depend only upon the volume fraction of particles present, Φ_a. For spherical particles, the simplest dependence is described by Einstein's model [14]:

$$\frac{\mu}{\mu_0} = 1 + 2.5\Phi_a \tag{2.4}$$

which has been shown to predict the viscosity at very small volume fractions, $\Phi_a < 0.02$, but underpredicts the viscosity at higher concentrations [1]. For larger volume fractions $\Phi_a < 0.2$, Abedian and Kachanov [1] found that the viscosity is better predicted by

$$\frac{\mu}{\mu_0} = (1 - 2.5\Phi_a)^{-1}. \tag{2.5}$$

Combining all independent functions, the viscosity is defined as

$$\mu(\theta, \Phi_a) = \mu_0(1 - 2.5\Phi_a)^{-1}\exp\left[\frac{E_\theta}{R\theta}\right] \tag{2.6}$$

2.3 Governing Equations

2.3.1 Thermal Governing Equations

To solve the thermal problem, we start with the energy balance equation. Assuming there is no increase in heating due to internal stresses and heat conduction is governed by Fourier's Law, the energy balance takes the form

$$\rho c\dot{\theta} = \nabla \cdot (\mathbb{K}\nabla\theta) + Q \tag{2.7}$$

where ρ is density, c is specific heat, θ is tempeature, ∇ is the differential operator, $\mathbb{K}$ is thermal conductivity, and Q is heat generation. Heat is internally generated only during the curing process from the laser and the chemical reaction.

For the heated surface, such as the build platform, Dirichlet boundary conditions are applied by directly specifying the temperature

$$\theta = \bar{\theta}. \tag{2.8}$$

For all other surface, it is assumed that no heat will be lost through convection and thus the flux boundary condition is

$$-\mathbb{K}\nabla_n\theta = \mathbf{q}_n = 0. \tag{2.9}$$

2.3.2 Mechanical Governing Equations

The mechanical problem is solved using the governing equations for the conservation of mass and momentum. Writing the governing equation in Lagrangian form the balance of linear momentum is

$$\rho\frac{D\mathbf{v}}{Dt} = \nabla \cdot \mathbf{T} + \rho\mathbf{b} \tag{2.10}$$

where $\frac{D}{Dt}$ is the material time derivative, $\mathbf{v}$ is velocity, $\mathbf{T}$ is the Cauchy stress, and $\mathbf{b}$ is any body forces. The conservation of mass is

$$\frac{D\rho}{Dt} + \rho\nabla \cdot \mathbf{v} = 0. \tag{2.11}$$

Since it is assumed that the polymer resin is incompressible, the conservation of mass simplifies to

$$\nabla \cdot \mathbf{v} = 0. \tag{2.12}$$

Using the incompressible linear viscous fluid given in Equation 2.1 and plugging into the balance of linear momentum, Equation 2.10, provides

$$\rho\frac{D\mathbf{v}}{Dt} = \rho\mathbf{b} - \nabla p + \nabla \cdot \left(2\mu(\nabla\mathbf{v})^s\right). \tag{2.13}$$

For domains in which the position is held fixed, i.e. the build platform, Dirichlet boundary conditions are applied, specifically, the velocity is set to zero

$$\mathbf{v} = \bar{\mathbf{v}} = 0. \tag{2.14}$$

For all other boundaries, surface tension is applied as a traction boundary condition

$$\mathbf{T} \cdot \mathbf{n} = \bar{\mathbf{t}} = \gamma \kappa \mathbf{n} \tag{2.15}$$

where γ is the surface tension coefficient and κ is the surface curvature. The curvature of the surface at a given point is approximated by connecting the current point of interest with a circle or sphere with the two or three neighbors it shares a boundary with for two- and three-dimensional problems respectively [29, 37]. The curvature is then defined by the inverse of the radius, $\kappa = \frac{1}{||\mathbf{R}||}$, and the normal to the surface is defined by the direction of the center, $\mathbf{n} = \frac{\mathbf{R}}{||\mathbf{R}||}$, Figure 2.2. Plugging into the traction boundary condition provides

$$\mathbf{T} \cdot \mathbf{n} = \gamma \frac{\mathbf{R}}{||\mathbf{R}||^2}. \tag{2.16}$$

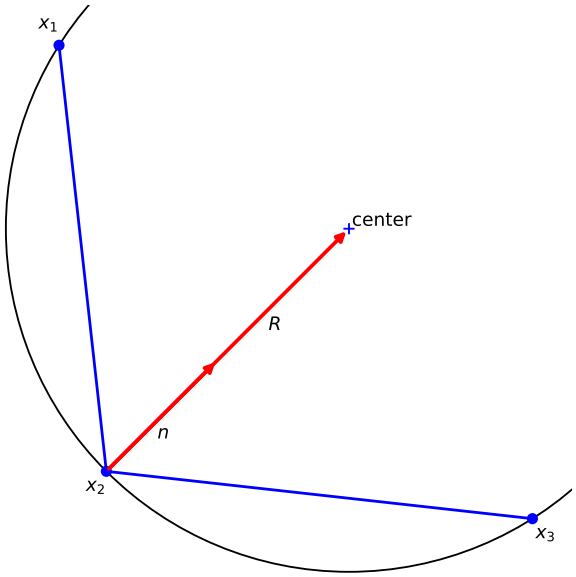

Figure 2.2: Example normal calculation for surface tension boundary condition.

2.4 Boundary Identification and Mesh Generation

A key component to PFEM is the regeneration of the mesh at every time step based upon the position of the points. In this work, a triangular mesh in two-dimensions and tetrahedral mesh in three-dimensions is generated through Delaunay triangulation [4]. One of the limitations of Delaunay triangulation is that it inherently generates a domain with a convex boundary and all points are connected to a single domain. To address this, prior to meshing the domain the boundaries are idenfitied using the α-shape method [13, 44], allowing for nonconvex boundaries and separation of material fundamental to PFEM.

To implement the α-shape method, first define the boundary of a set of points, or particles, as a series of elements connecting a subset of points on the boundary. The subset is composed of two points in two-dimensions and three points in three-dimensions. In two-dimensions each subset is identified by connecting any two points with a circle. The radius of the circle is predefined by the minimum distance between any two points and a constant α. If no other point exists within the circle, the line between the pair of points defines a boundary. This is easily expanded to three-dimension by connecting three points by a sphere. In both cases, the α-shape method provides two conditions that must be satisfied to determine a boundary element; the distance between the points cannot exceed the diameter of the circle, or sphere, and no other point can exist within the circle, or sphere. Figure 2.3 illustrates the search for the boundary in a two-dimensional domain. Once the boundaries are identified and the interior of each domain is meshed and the numeric problem is solved using the finite element algorithm described in this work.

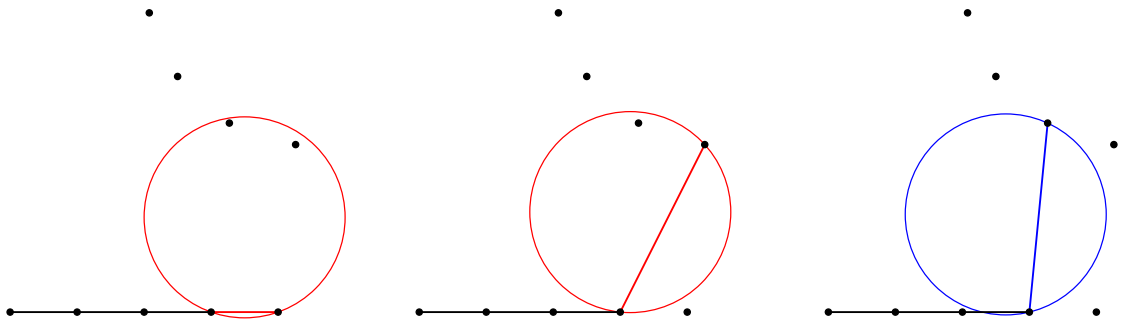

Figure 2.3: Example of two-dimensional boundary detection in which the α-shape conditions for boundary detection are violated, (a) and (b), and satisfied (c).

2.5 Discretization of Governing Equations

2.5.1 Shape Functions

The variables that require discretization are any which are associated with the particles, specifically temperature, θ, heat generation, Q, velocity, $\mathbf{v}$, and pressure, p. Pressure and heat generation are included as nodal values since each particle represents the material and not the elements themselves.

Since the mesh is generated through triangulation between particles, the approximation of each variable within the elements is achieved through linear shape functions, $\mathbf{N}$. For triangular and tetrahedral elements, linear shape functions correspond to the area and volume coordinates respectively. At any given point in an element, the approximation for each variable takes the form

$$\begin{aligned} \theta &= \sum_j N_j \theta_j \\ Q &= \sum_j N_j Q_j \\ p &= \sum_j N_j p_j \\ v_i &= \sum_j N_j v_{ji} \end{aligned} \tag{2.17}$$

where j corresponds to each node of the element and i is the spacial dimension. In matrix form the approximations become

$$\begin{aligned} \theta &= \mathbf{N}\boldsymbol{\Theta} \\ Q &= \mathbf{N}\mathbf{Q} \\ p &= \mathbf{N}\mathbf{P} \\ v_i &= \mathbf{N}\mathbf{V}_i \end{aligned} \tag{2.18}$$

where in three-dimensions $\mathbf{N} = [N_1\, N_2\, N_3\, N_4]$ and $\boldsymbol{\Theta}$, $\mathbf{Q}$, $\mathbf{P}$, and $\mathbf{V}_i$ take the form of $\mathbf{X} = [X_1\, X_2\, X_3\, X_4]^T$. To reduce the number of terms, the velocity approximation is written in a more compact form as

$$\mathbf{v} = \mathbf{N}_v \mathbf{V} = [N_1\mathbf{I} \quad N_2\mathbf{I} \quad N_3\mathbf{I} \quad N_4\mathbf{I}]\, \mathbf{V} \tag{2.19}$$

where $\mathbf{I}$ is the 3×3 identity tensor, $\mathbf{N}_v$ is a 3×12 shape function tensor, and $\mathbf{V} = [V_{11}\, V_{12}\, V_{13}\, V_{21}\, V_{22}\, V_{23}\, V_{31}\, V_{32}\, V_{33}\, V_{41}\, V_{42}\, V_{43}]^T$.

2.5.2 Discretization of Thermal Equations

Discretization of the energy balance is achieved by applying the method of weighted residuals:

$$\int_\Omega \mathbf{N}^T \rho c \dot{\theta} \mathrm{d}\Omega = \int_\Omega \mathbf{N}^T \nabla \cdot (\mathbb{K} \nabla \theta) \mathrm{d}\Omega + \int_\Omega \mathbf{N}^T Q \mathrm{d}\Omega - \int_{\Gamma_n} \mathbf{N}^T \left(\mathbb{K} \nabla \theta \cdot \mathbf{n} + \mathbf{q}_n \right) \mathrm{d}\Gamma. \tag{2.20}$$

Using integration by parts and the divergence theorem, the weak form becomes

$$\int_\Omega \mathbf{N}^T \rho c \dot{\theta} \mathrm{d}\Omega = - \int_\Omega \nabla \mathbf{N}^T \mathbb{K} \nabla \theta \mathrm{d}\Omega + \int_\Omega \mathbf{N}^T Q \mathrm{d}\Omega - \int_{\Gamma_n} \mathbf{N}^T \mathbf{q}_n \mathrm{d}\Gamma. \tag{2.21}$$

Plugging in the discretization of θ and Q provides

$$\int_\Omega \mathbf{N}^T \rho c \mathbf{N} \mathrm{d}\Omega \dot{\mathbf{\Theta}} = - \int_\Omega \nabla \mathbf{N}^T \mathbb{K} \nabla \mathbf{N} \mathrm{d}\Omega \mathbf{\Theta} + \int_\Omega \mathbf{N}^T \mathbf{N} \mathrm{d}\Omega \mathbf{Q} - \int_{\Gamma_n} \mathbf{N}^T \mathbf{q}_n \mathrm{d}\Gamma. \tag{2.22}$$

In matrix notation the discretized energy balance equation becomes

$$\mathbf{C} \dot{\mathbf{\Theta}} = -\mathbf{L} \mathbf{\Theta} + \mathbf{F}_\theta. \tag{2.23}$$

An implicit time stepping scheme is applied to the discretization to allow for any time step size physically permissible by the mechanical equations. This results in the discretized equation becoming

$$\frac{1}{\Delta t} \mathbf{C} \left(\mathbf{\Theta}_{n+1} - \mathbf{\Theta}_n \right) = -\mathbf{L} \mathbf{\Theta}_{n+1} + \mathbf{F}_\theta. \tag{2.24}$$

Finally, solving for the temperature at the next time step, $\mathbf{\Theta}_{n+1}$, provides

$$\left(\mathbf{C} + \Delta t \mathbf{L} \right) \mathbf{\Theta}_{n+1} = \mathbf{C} \mathbf{\Theta}_n + \Delta t \mathbf{F}_\theta. \tag{2.25}$$

2.5.3 Discretization of Mechanical Equations

A common method for solving the system of equations provided by the balance of linear momentum and conservation of mass, Equations 2.13 and 2.12, is the projection method introduced by Chorin [8, 9, 27, 28]. This method follows three steps, first solve the balance of linear momentum without pressure to calculate an intermediate ficticous velocity, $\mathbf{v}^*$. The ficticous velocity is not divergence free, $\nabla \cdot \mathbf{v}^* \neq 0$, so the pressure is calculated so that the velocity at the next time step satisfies the divergence free condition. Finally, the ficticous velocity is corrected to solve for the velocity. For each time step, the system of equations to solve becomes

$$\frac{\rho}{\Delta t} \mathbf{v}^* - \nabla \cdot (2\mu (\nabla \mathbf{v}^*)^s) = \frac{\rho}{\Delta t} \mathbf{v}_n + \rho \mathbf{b} \tag{2.26a}$$

$$\frac{\Delta t}{\rho} \nabla \cdot \nabla p_{n+1} = \nabla \cdot \mathbf{v}^* \tag{2.26b}$$

$$\mathbf{v}_{n+1} = \mathbf{v}^* - \frac{\Delta t}{\rho} \nabla p_{n+1}. \tag{2.26c}$$

With the newly separated equations, the discretization process applied to the thermal problem is applied to each equation. Starting with Equation 2.26a, applying the method of weighted residuals providing the weak form

$$\begin{aligned}\frac{1}{\Delta t}\int_\Omega \mathbf{N}_v^T \rho \mathbf{v}^* \mathrm{d}\Omega - \int_\Omega \mathbf{N}_v^T \nabla \cdot \left(2\mu \left(\nabla \mathbf{v}^*\right)^s\right) \mathrm{d}\Omega \\ = \frac{1}{\Delta t}\int_\Omega \mathbf{N}_v^T \rho \mathbf{v}_n \mathrm{d}\Omega + \int_\Omega \mathbf{N}_v^T \rho \mathbf{b} \mathrm{d}\Omega + \int_{\Gamma_n} \mathbf{N}_v^T \left(\bar{\mathbf{t}} - \left(2\mu \left(\nabla \mathbf{v}^*\right)^s\right) \cdot \mathbf{n}\right) \mathrm{d}\Gamma.\end{aligned} \tag{2.27}$$

Using integration by parts and the divergence theorem, the weak form becomes

$$\begin{aligned}\frac{1}{\Delta t}\int_\Omega \mathbf{N}_v^T \rho \mathbf{v}^* \mathrm{d}\Omega + \int_\Omega \nabla \mathbf{N}_v^T 2\mu \left(\nabla \mathbf{v}^*\right)^s \mathrm{d}\Omega \\ = \frac{1}{\Delta t}\int_\Omega \mathbf{N}_v^T \rho \mathbf{v}_n \mathrm{d}\Omega + \int_\Omega \mathbf{N}_v^T \rho \mathbf{b} \mathrm{d}\Omega + \int_{\Gamma_n} \mathbf{N}_v^T \bar{\mathbf{t}} \mathrm{d}\Gamma.\end{aligned} \tag{2.28}$$

Plugging the discretization of $\mathbf{v}$ provides

$$\begin{aligned}\frac{1}{\Delta t}\int_\Omega \mathbf{N}_v^T \rho \mathbf{N}_v \mathrm{d}\Omega \mathbf{V}^* + \int_\Omega \nabla \mathbf{N}_v^T 2\mu \left(\nabla \mathbf{N}_v \mathbf{V}^*\right)^s \mathrm{d}\Omega \\ = \frac{1}{\Delta t}\int_\Omega \mathbf{N}_v^T \rho \mathbf{N}_v \mathrm{d}\Omega \mathbf{V}_n + \int_\Omega \mathbf{N}_v^T \rho \mathbf{b} \mathrm{d}\Omega + \int_{\Gamma_n} \mathbf{N}_v^T \bar{\mathbf{t}} \mathrm{d}\Gamma.\end{aligned} \tag{2.29}$$

The symmetric limitation in the second term is removed by replacing the multiplicative two with a matrix, $\mathbf{D}$, resulting in

$$\begin{aligned}\frac{1}{\Delta t}\int_\Omega \mathbf{N}_v^T \rho \mathbf{N}_v \mathrm{d}\Omega \mathbf{V}^* + \int_\Omega \nabla \mathbf{N}_v^T \mu \mathbf{D} \nabla \mathbf{N}_v \mathrm{d}\Omega \mathbf{V}^* \\ = \frac{1}{\Delta t}\int_\Omega \mathbf{N}_v^T \rho \mathbf{N}_v \mathrm{d}\Omega \mathbf{V}_n + \int_\Omega \mathbf{N}_v^T \rho \mathbf{b} \mathrm{d}\Omega + \int_{\Gamma_n} \mathbf{N}_v^T \bar{\mathbf{t}} \mathrm{d}\Gamma\end{aligned} \tag{2.30}$$

where

$$\mathbf{D} = \begin{bmatrix} 2 & 0 & 0 & 0 & 0 & 0 \\ 0 & 2 & 0 & 0 & 0 & 0 \\ 0 & 0 & 2 & 0 & 0 & 0 \\ 0 & 0 & 0 & 1 & 0 & 0 \\ 0 & 0 & 0 & 0 & 1 & 0 \\ 0 & 0 & 0 & 0 & 0 & 1 \end{bmatrix}. \tag{2.31}$$

In matrix notation this becomes

$$\frac{1}{\Delta t}\mathbf{M}\mathbf{V}^* + \mathbf{K}\mathbf{V}^* = \frac{1}{\Delta t}\mathbf{M}\mathbf{V}_n + \mathbf{F}_t. \tag{2.32}$$

Next the velocity correction equation, 2.26c, is discretized. Applying the method of weighted residuals gives the weak form

$$\frac{1}{\Delta t}\int_\Omega \mathbf{N}_v^T \rho \mathbf{v}_{n+1} \mathrm{d}\Omega - \frac{1}{\Delta t}\int_\Omega \mathbf{N}_v^T \rho \mathbf{v}^* \mathrm{d}\Omega = -\int_\Omega \mathbf{N}_v^T \nabla p_{n+1} \mathrm{d}\Omega. \tag{2.33}$$

Plugging in the discretization of $\mathbf{v}$ and p provides

$$\frac{1}{\Delta t}\int_\Omega \mathbf{N}_v^T \rho \mathbf{N}_v \mathrm{d}\Omega \mathbf{V}_{n+1} = \frac{1}{\Delta t}\int_\Omega \mathbf{N}_v^T \rho \mathbf{N}_v \mathrm{d}\Omega \mathbf{V}^* - \int_\Omega \mathbf{N}_v^T \nabla \mathbf{N} \mathrm{d}\Omega \mathbf{P}_{n+1}. \tag{2.34}$$

In matrix notation this becomes

$$\mathbf{M}\mathbf{V}_{n+1} = \mathbf{M}\mathbf{V}^* - \Delta t \mathbf{B}\mathbf{P}_{n+1}. \tag{2.35}$$

The final equation to discretize is the pressure calculation of Equation 2.26b. The method of weighted residuals gives

$$\int_\Omega \mathbf{N}^T \nabla \cdot \mathbf{v}^* \mathrm{d}\Omega - \int_\Omega \mathbf{N}^T \frac{\Delta t}{\rho} \nabla \cdot \nabla p_{n+1} \mathrm{d}\Omega = 0. \tag{2.36}$$

Performing integration by parts results in the weak form becoming

$$\begin{aligned}\int_\Omega \nabla \cdot \left(\mathbf{N}^T \mathbf{v}^*\right) \mathrm{d}\Omega - \int_\Omega \nabla \mathbf{N}^T \mathbf{v}^* \mathrm{d}\Omega \\ - \int_\Omega \nabla \cdot \left(\mathbf{N}^T \frac{\Delta t}{\rho} \nabla p_{n+1}\right) \mathrm{d}\Omega + \int_\Omega \nabla \mathbf{N}^T \frac{\Delta t}{\rho} \nabla p_{n+1} \mathrm{d}\Omega = 0.\end{aligned} \tag{2.37}$$

This can be simplified to

$$\int_\Omega \nabla \cdot \left(\mathbf{N}^T \left(\mathbf{v}^* - \frac{\Delta t}{\rho} \nabla p_{n+1}\right)\right) \mathrm{d}\Omega - \int_\Omega \nabla \mathbf{N}^T \mathbf{v}^* \mathrm{d} + \int_\Omega \nabla \mathbf{N}^T \frac{\Delta t}{\rho} \nabla p_{n+1} \mathrm{d}\Omega = 0. \tag{2.38}$$

Using Equation 2.26c the first term becomes

$$\int_\Omega \nabla \cdot \left(\mathbf{N}^T \left(\mathbf{v}^* - \frac{\Delta t}{\rho} \nabla p_{n+1}\right)\right) \mathrm{d}\Omega = \int_\Omega \nabla \cdot \left(\mathbf{N}^T \mathbf{v}_{n+1}\right) \mathrm{d}\Omega. \tag{2.39}$$

Recalling that in the method of weighted residuals $\mathbf{N}^T$ represents an arbirary constant, Equation 2.39 becomes zero since $\nabla \cdot \left(\mathbf{N}^T \mathbf{v}_{n+1}\right) = 0$. This results in the weak form becoming

$$\int_\Omega \nabla \mathbf{N}^T \mathbf{v}^* \mathrm{d}\Omega = \int_\Omega \nabla \mathbf{N}^T \frac{\Delta t}{\rho} \nabla p_{n+1} \mathrm{d}\Omega. \tag{2.40}$$

Plugging in the discretization of $\mathbf{v}$ and p provides

$$\int_\Omega \nabla \mathbf{N}^T \mathbf{N}_v \mathrm{d}\Omega \mathbf{V}^* = \int_\Omega \nabla \mathbf{N}^T \frac{\Delta t}{\rho} \nabla \mathbf{N} \mathrm{d}\Omega \mathbf{P}_{n+1}. \tag{2.41}$$

The first integral term is recognized as $\mathbf{B}^T$ while the second integral term can be calculated using $\Delta t \mathbf{B}^T \mathbf{M}^{-1} \mathbf{B}$, this results in the final equation being written as

$$\mathbf{B}^T \mathbf{V}^* = \Delta t \mathbf{B}^T \mathbf{M}^{-1} \mathbf{B} \mathbf{P}_{n+1}. \tag{2.42}$$

2.6 Numeric Algorithm

To implement the PFEM as described in Section 2.1, first consider solving for a single time step. Notating the particle parameters with a subscript n corresponding to the time step and a superscript i corresponds to the iteration step, the process is as follows:

---

1. Begin with particles in the known configuration at time step n

$$\mathbf{X}_n,\ \mathbf{V}_n,\ \mathbf{\Theta}_n$$

2. Use the current positions as the initial guess for the position at the next time step

$$\mathbf{X}^0_{n+1} = \mathbf{X}_n$$

3. Begin loop over iterative solver i

   a) Identify boundaries and mesh domain based upon new position, $\mathbf{X}^i_{n+1}$

   b) Calculate the velocity estimate, $\mathbf{V}^*$, Equation 2.32

$$(\mathbf{M} + \Delta t\mathbf{K})\,\mathbf{V}^* = \mathbf{M}\mathbf{V}_n + \Delta t\mathbf{F}_t$$

   c) Calculate the pressure, $\mathbf{P}_{n+1}$, Equation 2.42

$$\Delta t\mathbf{B}^T\mathbf{M}^{-1}\mathbf{B}\mathbf{P}_{n+1} = \mathbf{B}^T\mathbf{V}^*$$

   d) Calculate the corrected velocity, $\mathbf{V}^{i+1}_{n+1}$, Equation 2.35

$$\mathbf{M}\mathbf{V}_{n+1} = \mathbf{M}\mathbf{V}^* - \Delta t\mathbf{B}\mathbf{P}_{n+1}$$

   e) Calculate the new position of the particles, $\mathbf{X}^{i+1}_{n+1}$, using

$$\mathbf{X}^{i+1}_{n+1} = \mathbf{X}_n + \mathbf{V}^{i+1}_{n+1}\Delta t$$

   f) Calculate the temperature, $\mathbf{\Theta}_{n+1}$, Equation 2.25

$$(\mathbf{C} + \Delta t\mathbf{L})\,\mathbf{\Theta}_{n+1} = \mathbf{C}\mathbf{\Theta}_n + \Delta t\mathbf{F}_\theta$$

   g) Update viscosity, μ, Equation 2.6

$$\mu(\theta, \Phi_a) = \mu_0(1 - 2.5\Phi_a)^{-1}\exp\left[\frac{E_\theta}{R\theta_{n+1}}\right]$$

h) Do all variables converge

$$\left\|\mathbf{Z}_{n+1}^{i+1} - \mathbf{Z}_{n+1}^{i}\right\| <= 10^{-5} \left\|\mathbf{Z}_{n}\right\| \tag{2.43}$$

$\rightarrow$ No $\rightarrow$ Return to step 3 and perform next iteration, $i \rightarrow i+1$
$\rightarrow$ Yes $\rightarrow$ Return to step 1 and perform next time step, $n \rightarrow n+1$

An iterative solver is implemented at each time step, Step 3, since the discretized equations are written using a Lagrangian formulation. This requries that the discretized equations are solved on the mesh at the next time step but due to the remeshing process, the mesh at the next time step is unknown. To address this problem, the next mesh is approximated as being the same as the previous and the position of each particle is determined. By calculating the error between the previous and new estimate for the particle positions, we can find a convergent solution for the new position of the particles.

Another important consideration is the time step size. It is possible that due to the physics of the problem, the time step size implemented is too large. Two of the challenges that can arise due to a time step that is too large are, (1) two materials can completely passing each other without interacting, Figure 2.4b, and (2) the estimates for the next mesh may result in interpenetraiton of two materials that merge prior to interaction and thus a convergent solution cannot be found, Figure 2.4c.

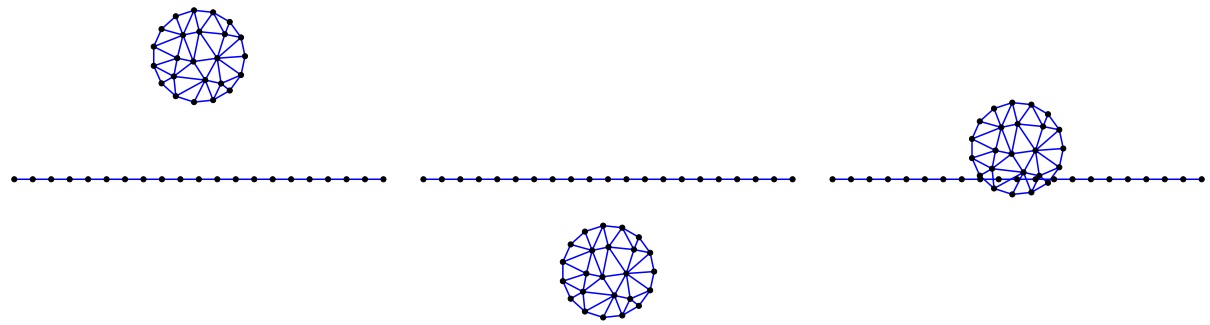

Figure 2.4: (a) Initial domain before moving the mesh, (b) a time step too large that the moving domain passes the fixed domain, and (c) a smaller time step still too large that the domains merge before interacting.

To address the first challenge, the maximum permissible time step is taken as the minimum value between a user specified maximum, dt_{user}, and the ratio between the minimum spacing, ds_{min}, and norm of the maximum velocity, $||\mathbf{v}||_{max}$, specifically

$$dt_{max} = \min(dt_{user}, \frac{ds_{min}}{||\mathbf{v}||_{max}}). \tag{2.44}$$

This limits how far any one particle can move to be the minimum spacing between any two particles and thus ensuring that two domains will always come into contact before they pass each other. To prevent a waste of computational time, all particle domains start in close proximity.

The second challenge is addressed by limiting the number of interation, i, performed at a given time step. If a convergent solution cannot be found within the specified number of iterations, the time step size is halved and the algorithm returns to Step 1 without incrementing n.

While beneficial to ensuring a convergent solution is obtained, only decreasing the time step can result in the unnecessary iterations and increased computational time. An example of this is a droplet as it moves without coming into contact with any other surface. To avoid unnecessary calculations, once a convergent solution is obtained the time step size is increased by a factor of 1.25 up to the maximum allowable value prior to returning to Step 1 and solving for the next time step, $n + 1$.

Chapter 3

Photopolymer Curing Model

3.1 Free-Radical Polymerization

To include the chemical solidification process to the particle finite element method (PFEM), an analytical model for the polymerization process is introduced. The typical curing process for photopolymers in additive manufacturing is free-radical polymerization. As a chain-reaction polymerization process, there are four distinct steps [39]. These steps are:

1. Chain initiation - The process in which a chemical reaction induced by the introduction of an energy source, causes the formation of a free-radical that converts a monomer into a highly reactive molecule allowing for chain growth. These reactive molecules are referred to as active chains.

2. Chain propagation - The process in which free monomers react with the active chains resulting in chain growth and the formation of a new active site.

3. Chain transfer - The process in which an active chain and second molecule, such as a free monomer, react terminating the active chain and creating a new reactive molecule.

4. Chain termination - The process in which two active chains react resulting in termination of both chains. The termination can happen through combination, two chains forming a single polymer chain, or through disproportionation, two chains react forming two separate polymer chains.

In the model presented in this work, the chain transfer step is neglected for two reasons. First, the rate at which the chain transfer occurs is small compared to other rate terms and thus has a negligible impact on decreasing the rate of chain propagation. Second, the specific molecular weight of each chain is not considered and thus understanding specificially when a given chain terminates is not neccessary. The modified polymerization process can be schematically shown as:

$$S \xrightarrow{k_d} 2R\cdot$$
$$R\cdot + M \xrightarrow{k_i} M_1\cdot \qquad \text{Chain Initiation} \tag{3.1a}$$

$$M_n\cdot + M \xrightarrow{k_p} M_{n+1}\cdot \qquad \text{Chain Propagation} \tag{3.1b}$$

$$M_m\cdot + M_n\cdot \begin{cases} \xrightarrow{k_{tc}} M_{m+n} \\ \xrightarrow{k_{td}} M_m + M_n \end{cases} \qquad \text{Chain Termination} \tag{3.1c}$$

In this schematic k_j is the rate constant for each reaction, S is the photoinitiator, $R\cdot$ is the initiating free-radical, M is a single monomer, $M_n\cdot$ is an active chain, and M_m is the polymer chain with degree of polymerization m.

The simplest and most common method for characterizing the polymerization process is by measuring the degree of cure, or the percentage of the monomer that has been converted into polymer chains. The degree of cure is calculated as

$$C = 1 - \frac{[M]}{[M]_0} \tag{3.2}$$

where C is the degree of cure, $[M]$ is the current concentration of the monomer, and $[M]_0$ is the initial concentration. The value for the degree of cure is bound between 0 and 1 with $C = 0$ representing to the uncured resin and $C = 1$ representing the idealized fully cured polymer.

In the remainder of this chapter, the rate equations for change in concentrations of the various constituents, specifically the photoinitiator, monomer, and active chains, is covered in Section 3.2. Next the dependency of the rate constants on the temperature and mobility of the constitutents is covered in Section 3.3. Since the polymerization process is exothermic, Section 3.4 covers the equations for heat generation to be included in the energy balance. The next two sections, Sections 3.5 and 3.6, cover the discretization of the light intensity and rate equations, respectively. Finally, Section 3.7 provides an overview of the algorithm for solving the system of equations.

3.2 Rate Equations

To determine the degree of cure within the material, we require knowing the current concentration of unreacted monomer. The current concentration is calculated by considering the rate at which the concentration changes. The factors influencing the rate of change are diffusion of monomer through the domain and consumption of monomer during active chain formation and propagation. This leads to an equation of the form

$$\frac{d[M]}{dt} = D_m \nabla^2 [M] - R_i - R_p \tag{3.3}$$

where D_M is the diffusion constant for the monomer, R_i is the rate of initation of active chains, and R_p is the rate of propagation, or the rate at which monomer is consumed during polymerizaiton. Typical photopolymers are composed of only one to five weight percent of the initiator [47] thus the monomer consumed by the initiation process is small compared to the concentration consumed during chain propagation. This means that the rate of initiation can be neglected resulting in the monomer concentration changing at a rate of

$$\frac{d[M]}{dt} = D_m \nabla^2 [M] - R_p. \tag{3.4}$$

The diffusion coefficient for the monomer is dependent upon the temperature and the degree of cure. As the temperature increases the free volume for motion increases allowing for more diffusion. On the other hand, as the material cures, mobility is decreased around the longer polymer chains. To account for both of these behaviors, the diffusion constant is given by the equation

$$D_m = D_{m,0} \exp\left[\frac{-A_m}{f}\right] \tag{3.5}$$

where $D_{m,0}$ is the pre-exponential factor, A_m is the parameter characterizating the rate at which the diffusion rate decreases, and f is the fractional free volume. The fractional free volume captures both the degree of cure and temperature dependence of the diffusion constant and will be discussed in more detail in Section 3.3.

From the schematic for chain propagation, Equation 3.1b, the rate at which monomer is consumed during polymerization is proportional to the concentration of the monomer and active chains resulting in

$$R_p = k_p [M][M\cdot] \tag{3.6}$$

where k_p is the rate constant for propagation and $[M\cdot]$ is the concentration of the active chains. Plugging in the rate of propagation provides a rate of change in the monomer concentration of

$$\frac{d[M]}{dt} = D_m \nabla^2 [M] - k_p [M][M\cdot]. \tag{3.7}$$

To calculate the current monomer concentration, we require the current concentration of active chains, $[M\cdot]$. The concentration of active chains is dependent upon the rate at which

active sites are formed and at which they react to terminate. This is written as

$$\frac{d[M\cdot]}{dt} = R_i - R_t \tag{3.8}$$

where R_i is the rate of initation of active chains and R_t is the rate of termination. This rate equation does not provide the degree of polymerization of each individual polymer chain, but rather the concentration of active chains within the system. The degree of polymerization is neglected as we are presently interested in the extent to which the polymer has cured versus the detailed microstructural properties. Note that oxygen inhibition of active chains is neglected though could be accounted for through the introduction of an additional rate term.

The first term, initiation of polymerization, corresponds to an increase in the active chain concentration due to photoinitiator produced free-radicals reacting with the monomer, schematically shown in Equation 3.1a. Due to the small concentration of photoinitiators, it is assumed that all free-radicals react with the monomer almost instantaneously. This means the rate of initiation is equivalent to the rate of free-radical formation. Assuming that each photoinitiator produces two free-radicals the rate of initiation is given by

$$R_i = 2\phi I_a \tag{3.9}$$

where ϕ is quantum yield of initiation and I_a is the light absorbed by the photoinitiators. The light absorbed by the photoinitators is given by

$$I_a = \epsilon_s[S]I \tag{3.10}$$

where ϵ_s is initiator absorbtivity, $[S]$ is the concentration of the initiator, and I is the light intensity.

The second term, termination of polymerization, corresponds to a decrease in the active chain concentration due to the reaction between two active chains, Equation 3.1c. Although two methods of termination are illustrated, as single term characterizes the termination process as

$$R_t = 2k_t[M\cdot]^2 \tag{3.11}$$

where $k_t = k_{tc} + k_{td}$ is the rate constant for termination.

Plugging the rate of initiation and termination into the active chain concentration rate equation gives

$$\frac{d[M\cdot]}{dt} = 2\phi\epsilon_s[S]I - 2k_t[M\cdot]^2. \tag{3.12}$$

Observe that after the light source has passed over a region, $I \to 0$, the concentration of the active chains remains nonzero for a period of time allowing for polymerization to continue.

Next, it is necessary to calculate the concentration of the photoinitiators, $[S]$, and light intensity, I. Since it is assumed that each photoinitiator produces two free-radicals, the

decrease in photoinitiator concentration is half the rate of active chain formation, R_i giving a rate equation of

$$\frac{d[S]}{dt} = -0.5R_i = -\phi\epsilon_s[S]I. \tag{3.13}$$

While the light intensity may also be a function of time, it is a known value at any given moment. So for the purpose of calculating the monomer concentration we use the Beer-Lambert law to characterize the light intensity through the material. The Beer-Lambert law provides

$$\frac{dI}{dz} = -I_{abs} = -\epsilon_y[Y]I \tag{3.14}$$

where z is a positive number representing the depth below the surface, I_{abs} is the light absorbed at the given depth, ϵ_y is the absorbtivity of material Y, and $[Y]$ is the concentration of material Y. For a pure photopolymeric system the light is only absorbed by the photoinitiators and thus Y becomes S for the photoiniator. The introduction of additives means that at any given point in the material, the light absorbed is dependent on the material present at the given depth and thus Y is either S for the photoinitiator or A for additive. Note that the optical effects, i.e. scattering, diffraction, refraction, and reflection, in the material and at the boundaries are neglected.

Using the light intensity and concentration of the photoinitiators and active chains, we can determine the monomer concentration. The concentration provided by Equation 3.7 results in the total change in concentration due to polymerization and diffusion. To calculate the degree of cure, we only want the concentration of the monomer consumed during polymerization as inclusion of diffusion results in both an over and under estimate of the degree of cure. The error in the estimations occur due to monomer diffusion out of regions of low polymerization, high monomer concentration, into regions of high polymerization, low monomer concentration. To correct for the diffusion term, the initial concentration in Equation 3.2 is replaced with a reference concentration which accounts for monomer diffusion. Specifically, the degree of cure becomes

$$C = 1 - \frac{[M]}{[M]^*} \tag{3.15}$$

where $[M]^*$ is the reference concentration and changes only as a rate of diffusion [23]

$$\frac{d[M]^*}{dt} = D_m\nabla^2[M]. \tag{3.16}$$

3.3 Kinetic Rate Constants

The rate constants, k_p and k_t, are dependent upon the temperature and mobility of monomers and active chains. During the early stages of polyermization, the increase in temperature is the driving force behind the change in the rate constants. As the temperature increases, the reactivity of the active chains increases, leading to an increase in the rate constant. The temperature dependence is thus introduced in the form of an Arrhenius type equation

$$k_p = A_p e^{-E_p/R\theta} \tag{3.17}$$

$$k_t = A_t e^{-E_t/R\theta} \tag{3.18}$$

where A_p and A_t are the pre-exponential factors, E_p and E_t are activation energies of the chemical reactions for propagation and termination, respectively, and R is the universal gas constant.

As polymerization continues, the increased chain length results in decreased mobility of the monomer and active chains. This means that local diffusion becomes the limiting factor for the rate constants. Goodner and Bowman [23, 24, 25] incorporated the diffusion controlled phenomena using the fractional free volume, f, by

$$k_p = \frac{k_{p0} e^{-E_p/R\theta}}{1 + e^{A_{Dp}(1/f - 1/f_{cp})}} \tag{3.19}$$

$$k_t = k_{t0} e^{-E_t/R\theta} \cdot \left[1 + \frac{1}{k_{t,r}/(k_{t0} e^{-E_t/R\theta}) + e^{-A_{Dt}(1/f - 1/f_{ct})}}\right]^{-1} \tag{3.20}$$

where A_{Dp} and A_{Dt} are parameters characterizating the rate at which the rate constants decrease, and f_{cp} and f_{ct} are the critical fractional free volumes. The critical fractional free volumes correspond to the point at which the rate constants transition from being limited by the rate at which the chemical reactions occur to the rate at which the monomer and active chains can diffuse through the material to react. Specifically, when f is above the critical value the rate constants are governed by the chemical reaction while when f is below the critical value the rate constants are governed by diffusion. Finally, $k_{t,r}$ is the rate of reaction diffusion characterized by the reactive site of active chains moving as a result of chain growth. The rate of reaction diffusion is given by

$$k_{t,r} = R_{rd} k_p [M] \tag{3.21}$$

where R_{rd} is the reaction diffusion parameter.

For the curing system, the fractional free volume is calculated using

$$f = f_m \Phi_m + f_p \Phi_p \tag{3.22}$$

$$f_m = f_{g,m} + \alpha_m(\theta - \theta_{gm}) \tag{3.23}$$

$$f_p = f_{g,p} + \alpha_p(\theta - \theta_{gp}) \tag{3.24}$$

where f_i is the fractional free volume, Φ_i is the volume fraction, $f_{g,i}$ is the fractional free volume at the glass transition temperature, α_i is the coefficient of thermal expansion, and θ_{gi} is glass transition temperature. The subscript m and p correspond to the pure monomer and pure polymer, respectively. Assuming that the fractional free volume of each component at the glass transition temperature is 0.025, the total fractional free volume is

$$f = 0.025 + \sum_{m,p} \Phi_i \alpha_i (\theta - \theta_{gi}). \tag{3.25}$$

The volume fraction of monomer, Φ_m, and monomer converted to polymer, Φ_p, are given by

$$\Phi_m = \frac{[M] MW_m}{\rho_m v_T} \tag{3.26}$$

$$\Phi_p = \frac{([M]_0 - [M]) MW_m}{\rho_p v_T} \tag{3.27}$$

where ρ_m and ρ_p are the densities of the monomer and polymer, respectively, and MW_M is the molecular weight of the monomer. v_T is a normalizing factor for the volume fractions to ensure that $\Phi_M + \Phi_P = 1$ and is given by

$$v_T = \frac{[M] MW_m}{\rho_m} + \frac{([M]_0 - [M]) MW_m}{\rho_p}. \tag{3.28}$$

3.4 Heat Generation During Polymerization

During the polymerization process, heat is generated through exothermic bond formation as the active chains propagate and the absorption of light by the photoinitiators. To account for this process, the heat generation term, Q, in the energy balance, Equation 2.7, becomes

$$Q = R_p \Delta H + I_a \tag{3.29}$$

where R_p is the rate of polymerization given by Equation 3.6, ΔH is the heat of polymerization, and I_a is the light absorbed by the photoinitiators given by Equation 3.10. Plugging in R_p and I_a results in the heat generation term becoming

$$Q = k_p [M][M\cdot] \Delta H + \epsilon_s [S] I. \tag{3.30}$$

The inclusion of the light absorbed assumes that the all the energy absorbed by the initiators is converted to heat. In reality, some of the energy goes to producing the free-radical through bond cleavage, but this quantity is negligible compared to energy dissipated as heat [23].

3.5 Discretization of Light Intensity

Before calculating any of the concentrations, the first task is to calculate the light intensity. From Equation 3.14 we observe that the intensity is a function of time due to the dependency on concentration of photoinitiators and additives. The time depencency is eliminated with two assumptions. First, the photoinitiators are non photobleaching, meaning that the initators absorb light even after activation. Second, since the initial concentration of photoinitiators is small the change in concentration of unactivated photoinitiators through diffusion is negligible. Applying both of these assumptions in the case of a pure photopolymer means that the light intensity becomes dependent only on the initial concentration of the photoinitiators, $[S]_0$. In the case of a composite material, the concentration of additives remains constant even as light is absorbed, thus $[A] = [A]_0$ for all time. This allows for the light intensity function given in Equation 3.14 to be rewritten as

$$\frac{dI}{dz} = -\epsilon_y [Y]_0 I. \tag{3.31}$$

The first step is to calculate the light intensity on the top surface using a gaussian distribution. The width and peak intensity are related to the height of the light source relative to the top surface. To calculate the intensity below the surface a backward difference is applied to the modified differential equation above, Equation 3.31, to obtain

$$\frac{I_{k+1} - I_k}{\Delta z} = -\epsilon_{y_{k+1}} [Y_{k+1}]_0 I_{k+1} \tag{3.32}$$

where I_{k+1} and Y_{k+1} are the light intensity and material of the particle located at $k+1$. Since z is the depth below the material surface, the subscript $k+1$ corresponds to the particle one layer below the particle located at k. Solving for I_{k+1} results in

$$I_{k+1} = I_k (1 + \Delta z \epsilon_{y_{k+1}} [Y_{k+1}]_0)^{-1}. \tag{3.33}$$

3.6 Discretization of Rate Equations

The dependencies between monomer, active chain, and photoinitiator concentrations to calculate the degree of cure requires that the first equation to be solved is the photoinitiator concentration. Since the inkjet printing process utilizes a moving light source, the light intensity is a function of time and thus an approximation through discretization is used in place of an explicit solution. Using an implicit time stepping for photoinitiator concentration, Equation 3.13 becomes

$$\frac{[S]_{n+1} - [S]_n}{\Delta t} = -\phi\epsilon_s[S]_{n+1}I_{n+1}. \tag{3.34}$$

Solving for $[S]_{n+1}$ results in

$$[S]_{n+1} = [S]_n(1 + \Delta t\phi\epsilon_s I_{n+1})^{-1}. \tag{3.35}$$

Next is the active chain concentration, using an implicit time stepping scheme, Equation 3.12 becomes

$$\frac{[M\cdot]_{n+1} - [M\cdot]_n}{\Delta t} = 2\phi\epsilon_s[S]_{n+1}I_{n+1} - 2k_t[M\cdot]^2_{n+1}. \tag{3.36}$$

Moving all terms to one side of the equality results in

$$2k_t\Delta t[M\cdot]^2_{n+1} + [M\cdot]_{n+1} - [M\cdot]_n - 2\phi\epsilon_s[S]_{n+1}I_{n+1}\Delta t = 0. \tag{3.37}$$

Solving for $[M\cdot]_{n+1}$ using the quadratic equation and keeping only the positive term gives

$$[M\cdot]_{n+1} = \frac{(1 + 8k_t\Delta tc)^{1/2} - 1}{4k_t\Delta t} \tag{3.38}$$

where $c = [M\cdot]_n + 2\phi\epsilon_s[S]_{n+1}I_{n+1}\Delta t$. Only the positive term is kept as a negative term corresponds to an unrealistic negative concentration.

To discretize the monomer concentration equation, the method of weighted residuals is applied the partial differential equation. Assuming there is no evaporation of the monomer, diffusion of the monomer across the boundaries is zero, specifically

$$D_m\nabla_n[M] = 0. \tag{3.39}$$

To apply the method of weighted residuals that is compatible with the mechanical and thermal discretizations, the concentration within each element is approximated with the linear shape functions, $\mathbf{N}$. For the monomer concentration this means writing the concentrations as

$$[M] = \sum_j N_j[M_j] = \mathbf{N}[\mathbf{M}] \tag{3.40}$$

where j corresponds to each node of the element. Using the same linear shape functions the method of weighted residuals applied to Equation 3.7 and the boundary condition results in

$$\begin{aligned}\int_\Omega \mathbf{N}^T[\dot{M}]\mathrm{d}\Omega = &\int_\Omega \mathbf{N}^T\nabla\cdot(D_m\nabla[M])\mathrm{d}\Omega \\ &- \int_\Omega \mathbf{N}^T k_p[M][M\cdot]\mathrm{d}\Omega - \int_{\Gamma_n}\mathbf{N}^T\left(D_m\nabla[M]\cdot\mathbf{n} + 0\right)\mathrm{d}\Gamma.\end{aligned} \tag{3.41}$$

Applying integration by parts and the divergence theorem provides the weak form

$$\int_\Omega \mathbf{N}^T[\dot{M}]\mathrm{d}\Omega + \int_\Omega \mathbf{N}^T k_p[M][M\cdot]\mathrm{d}\Omega + \int_\Omega \nabla\mathbf{N}^T D_m \nabla[M]\mathrm{d}\Omega = 0. \tag{3.42}$$

Before applying the monomer concentration discretization, first consider the treatment of $[M][M\cdot]$. For a single particle, the product is a scalar value so we can define it as $\mathbf{N}[\mathbf{M}][\mathbf{M}\cdot]$ where $[\mathbf{M}][\mathbf{M}\cdot] = [M_k][M_k\cdot]$ (no sum) is a term by term product. Applying the discretizations results in

$$\int_\Omega \mathbf{N}^T\mathbf{N}\mathrm{d}\Omega[\dot{\mathbf{M}}] + \int_\Omega \mathbf{N}^T k_p \mathbf{N}\mathrm{d}\Omega[\mathbf{M}][\mathbf{M}\cdot] + \int_\Omega \nabla\mathbf{N}^T D_m \nabla\mathbf{N}\mathrm{d}\Omega[\mathbf{M}] = 0. \tag{3.43}$$

Simplifying to matrix notation provides

$$\mathbf{C}_1[\dot{\mathbf{M}}] + \mathbf{C}_2[\mathbf{M}][\mathbf{M}\cdot] + \mathbf{L}_2[\mathbf{M}] = 0. \tag{3.44}$$

With the problem reformulated as an ordinary differential equation, we apply an implicit time stepping scheme to obtain

$$\frac{1}{\Delta t}\mathbf{C}_1\left([\mathbf{M}]_{n+1} - [\mathbf{M}]_n\right) + \mathbf{C}_2[\mathbf{M}]_{n+1}[\mathbf{M}\cdot]_{n+1} + \mathbf{L}_2[\mathbf{M}]_{n+1} = 0. \tag{3.45}$$

Solving for the new concentration, $[\mathbf{M}]_{n+1}$, provides

$$\left(\mathbf{C}_1 + \Delta t\mathbf{C}_2[\mathbf{M}\cdot]_{n+1} + \Delta t\mathbf{L}_2\right)[\mathbf{M}]_{n+1} = \mathbf{C}_1[\mathbf{M}]_n. \tag{3.46}$$

Note that the second term, $\mathbf{C}_2[\mathbf{M}\cdot]_{n+1}$, in index notation is $C_{2,jk}[M_k\cdot]_{n+1}$ (no sum).

Finally, to correct for diffusion in the calculation of the degree of cure, the same weighted residual discretization is applied to Equation 3.16. Since the correction to the reference concentration has the same general form as the change in monomer concentration, the matrix form of the discretized equation can be written as

$$\mathbf{C}_1[\dot{\mathbf{M}}]^* + \mathbf{L}_2[\mathbf{M}] = 0. \tag{3.47}$$

The primary differences between the discretizations is that the component due to curing, $\mathbf{C}_2[\mathbf{M}]_{n+1}[\mathbf{M}\cdot]_{n+1}$, is removed and that in the time dependent term the monomer concentration is replaced with the reference concentration $[\dot{\mathbf{M}}]^*$. Applying the implicit time stepping scheme and solving for the current reference concentration results in

$$\mathbf{C}_1[\mathbf{M}]^*_{n+1} = \mathbf{C}_1[\mathbf{M}]^*_n - \Delta t\mathbf{L}_2[\mathbf{M}]_{n+1}. \tag{3.48}$$

With the monomer and reference concentrations calculated, the degree of cure at each particle, i, is thus calculated using

$$C_{i,n+1} = 1 - \frac{[M]_{i,n+1}}{[M]^*_{i,n+1}}. \tag{3.49}$$

3.7 Curing Algorithm

The curing model can be introduced to the PFEM by simply adding it to the beginning of iterative solver after the domain is meshed but before solving the thermo-mechanical problem, Steps 3a and 3b of the PFEM algorithm. The curing model must be solved first since the polymerization process results in heat generation and would be missing from the thermal calculation if implemented afterward. The heat generated and degree of cure at the current time step is calculated using the following process:

---

1. Determine the light intensity, $\mathbf{I}_{n+1}$, Equation 3.33

$$I_{k+1,n+1} = I_{k,n+1}(1 + \Delta z \epsilon_{y_{k+1}}[Y_{k+1}]_0)^{-1}$$

2. Determine the initiator concentration, $[\mathbf{S}]_{n+1}$, Equation 3.35

$$[S_k]_{n+1} = [S_k]_n(1 + \Delta t \phi \epsilon_s I_{k,n+1})^{-1}$$

3. Determine the active chain concentration, $[\mathbf{M}\cdot]_{n+1}$, Equation 3.38

$$[M_k\cdot]_{n+1} = \frac{\left\{1 + 8k_t\Delta t\left([M_k\cdot]_n + 2\phi\epsilon_s[S_k]_{n+1}I_{k,n+1}\Delta t\right)\right\}^{1/2} - 1}{4k_t\Delta t}$$

4. Determine the monomer concentration, $[\mathbf{M}]_{n+1}$, Equation 3.46

$$\left(\mathbf{C}_1 + \Delta t\mathbf{C}_2[\mathbf{M}\cdot]_{n+1} + \Delta t\mathbf{L}_2\right)[\mathbf{M}]_{n+1} = \mathbf{C}_1[\mathbf{M}]_n$$

5. Determine the monomer reference concentration, $[\mathbf{M}]^*_{n+1}$, Equation 3.48

$$\mathbf{C}_1[\mathbf{M}]^*_{n+1} = \mathbf{C}_1[\mathbf{M}]^*_n - \Delta t\mathbf{L}_2[\mathbf{M}]_{n+1}$$

6. Determine the heat generated from the polymerization process, $\mathbf{Q}$, Equation 3.30

$$Q = k_p[M_k]_{n+1}[M_k\cdot]_{n+1}\Delta H + \epsilon_s[S_k]_0 I_{n+1}$$

7. Determine the degree of cure, $\mathbf{C}_{n+1}$, Equation 3.49

$$C_{k,n+1} = 1 - \frac{[M_k]_{n+1}}{[M_k]^*_{n+1}}$$

   where $C = 0$ corresponds to the uncured state and $C = 1$ is the fully cured state

---

In the case of a composite material, the algorithm remains unchanged, the only consideration is that the concentrations associated with the photopolymer, $[S]$, $[M\cdot]$, and $[M]$, are zero for all time in particles representing the additive.

Chapter 4

Investigation of Additive Effects

4.1 Modeling Overview

Two models are used to study the effects of additives on material behavior to develop an understanding of how additives change the material response during printing. The first model focuses on changes in the mechanical response of a single droplet. With out varying any of the process parameters, droplets with variable amounts of additives are deposited onto a surface. The second model focuses on the changes in the curing response of a composite material in an SLA type exposure to eliminate any influences of the process such as layer thickness and light source scan speed. Both of these simple models provide insight into the measurable variables to consider when determining the optimal process parameters for inkjet printing.

In both models, the amount of additive within the material is given as a weight fraction. This is due to the fact that experimental data is often given in weight fractions and thus the simulations being performed with weight fractions provides a more direct method for comparison. On the other hand, the computational algorithm presented in this work requires the volume fraction. Thus to convert between the weight fraction of additives, Ψ_a, and the volume fraction of additives, Φ_a, we use

$$\Phi_a = \frac{\Psi_a}{\Psi_a + (1 - \Psi_a)\frac{\rho_a}{\rho_m}} \tag{4.1}$$

where ρ_a is the density of the additive and ρ_m is the density of the matrix material.

For both models, the same materials are utilized. The photopolymer selected is 2-hydroxyethyl methacrylate (HEMA) with a 2,2-dimethoxy-2-phenylacetophenone (DMPA) photoinitiator due to both components being widely available and having a range of applications [2, 23, 47]. While many options exist for modifying the material properties, the additive selected is the cadmium selenide (CdSe) nanoparticle for the applications in electronics and biological imaging [56, 60]. The specific material properties utilized are provided in Table 4.1.

Table 4.1: Comprehensive list of material constants for inkjet printing models.

Parameter	Symbol	Value	Units
Volume fraction, additive	Φ_a	variable	
Volume fraction, monomer	Φ_m	variable	
Volume fraction, polymer	Φ_p	variable	
Density, additive	ρ_a	5820	kg / m^3
Density, initiator	ρ_s	1132	kg / m^3
Density, monomer	ρ_m	1073	kg / m^3
Density, polymer	ρ_p	1150	kg / m^3
Molecular weight, additive	MW_a	191.38	g /mol
Molecular weight, monomer	MW_m	130.14	g /mol
Molecular weight, initiator	MW_s	256.301	g /mol
Reference viscosity	μ_0	1.720×10^{-6}	Pa·s
Activiation energy, thermal	E_θ	26200	
Surface tension	γ	0.0485	N / m
Thermal conductivity	$\mathbb{K}$	0.2	W / m·K
Heat of polymerization	ΔH_p	54.8×10^3	W / mol
Heat capacity	c	1700	J / kg·K
Diffusion constant pre-exponential, monomer	$D_{m,0}$	2.36×10^{-6}	m^2 / s
Diffusion constant parameter, monomer	A_m	0.66	
Initiator absorptivity	ϵ_s	15×10^3	L / mol·m
Additive absorptivity	ϵ_a	9.15×10^2	L / mol·m
Quantum yield of initiation	ϕ	0.6	
Coefficient of thermal expansion, monomer	α_m	0.0005	1 / K
Coefficient of thermal expansion, polymer	α_p	0.000075	1 / K
Glass transition temperature, monomer	$\theta_{g,m}$	213	K
Glass transition temperature, polumer	$\theta_{g,p}$	328	K
True kinetic constant, polymerization	k_{p0}	1.6×10^6	L / mol·s
Activation energy, polymerization	E_p	18.23×10^3	J / mol
Diffusion parameter, polymerization	A_{Dp}	0.66	
Critical free volume, polymerization	f_{cp}	0.042	
True kinetic constant, termination	k_{t0}	3.6×10^6	L / mol·s
Activation energy, termination	E_t	2.94×10^3	J / mol
Diffusion parameter, termination	A_{Dt}	1.2	
Critical free volume, termination	f_{ct}	0.060	
Reaction diffusion parameter	R_{rd}	4	

In addition to the material properties, the initial concentrations of each of the photopolymer components and additive are shown in Table 4.2. Since each of the PFEM particles are either an additive or the photopolymer resin, the concentrations vary depending upon material type.

For the photopolymer resin, the initial concentration of the active chains is set to zero since there is no reaction until there is light exposure and the additive concentration is also set to zero since the materials are represented separately. The initial monomer and photoinitiator concentrations are determined using

$$[Y] = \frac{\rho_y}{MW_y}\Phi_y \tag{4.2}$$

where $[Y]$ is the concentration, ρ_y is the density, MW_y is the molecular weight, and Φ_y is the volume fraction of material Y. For this work, the weight fraction of photoinitiators is set to $\Psi_s = 0.035$.

For an additive particle, the concentrations for the monomer, photoinitiator, and active chains is zero and the concentration of the additive is calculated using

$$[A] = \frac{\rho_a}{MW_a} \tag{4.3}$$

with each of these values remaining unchanged at all times.

Table 4.2: List initial concentrations for the photopolymer and additive particles.

Parameter	Symbol	Value	Units
Monomer concentration	$[M]$	8.25	mol / L
Active chain concentration	$[M\cdot]$	0.0	mol / L
Photoinitiator concentration	$[S]$	0.15	mol / L
Additive concentration	$[A]$	30.4	mol / L

For all material information provided, it is assumed that the material is initially composed purely of monomers, photoinitiators, and additives. Materials utilized in inkjet printing require a higher viscosity that a pure monomer resin can provide and thus the primary component in the resin are oligomers. Monomers or low molecular weight oligomers are then added to reduce the viscosity and maintain a fluid system. A wax is also often added to induce a partial solidification during deposition through cooling [47]. The range of weight percents that can be contained within the inkjet printing resin are shown in Table 4.3.

Table 4.3: Range of weight percentages for the components in the photopolymer resin used by 3D Systems inkjet printers [47].

Component	Weight Percent
High molecular oligomer	$20 - 40$
Low molecular oligomer	$10 - 60$
Photoinitiator	$0.1 - 5$
Wax	$5 - 25$

To account for material being composed of oligomers and wax, the degree of cure is initially set to a nonzero value. Since specific molecular weights for the oligomers and wax vary from manufacturer to manufacturer and thus often explicitly unknown, the degree of cure is initially set to a value of 10%. HEMA has a gel point between 15 to 20% so an initial degree of cure of 10% corresponds to a still fluid material [35]. Note that the gel point is a measurable degree of cure in which the chain interactions overcome the ability for the material to flow and thus corresponds to a near solid phase. To implement the nonzero initial degree of cure, the reference monomer concentration remains as specified in Table 4.2 while the initial monomer concentration is modified to be 90% of reference value.

4.2 Droplet Impact Study

4.2.1 Overview of Objectives and Methodology

To study the changes in the mechanical response of composite materials the key processes parameters to be defined are ejection velocity, V_e, initial droplet temperature, θ_d, and build surface temperature, θ_b. To simplify the study the process parameters are fixed for all cases, specifically $V_e = 5.7$ m/s, $\theta_d = 85$ C, and $\theta_b = 40$ C. The ejection velocity is selected from the range of experimentally achievable velocities observed by Khalate et al. [31] while the temperatures were selected from the desired design range specified by 3D Systems United States patent number 6,841,589 [47].

To perform the single droplet impact study several considerations and assumptions are made to reduce computational time. Firstly, the ejection and flight behavior of the material are not considered. This impacts the model by assuming that the ejection velocity of the droplet out of the nozzle is the same velocity of the droplet as it approaches the build surface.

Additional, this leads to the assumption that the droplet is the same temperature just before impact as when it is released.

To demonstrate the effect of additives on deposition behavior, eight test cases are run, Table 4.4, the first case is a pure photopolymer system to serve as a baseline. In the seven remaining cases the weight fraction of the additive increases from 0.005 to 0.5.

Table 4.4: Test cases for effects of additives on a single droplet.

Test Case	1	2	3	4	5	6	7	8
Weight Fraction	0.0	0.005	0.01	0.02	0.05	0.1	0.2	0.5

One of the input files for the single droplet impact study is shown in Figure 4.1. The input file is generated by first determining the size of the droplet and particles. Since the size of a droplet typically ranges between 20 and 50 µm [11], the droplet diameters are selected to be 35 µm. The size of the particles are selected to correspond to the average size of the quantum dot additives utilized. After ejection, the quantum dots start to agglomerate together forming particles ranging in size from 1 to 50 µm [15]. Since the droplets are limited to 35 µm, the PFEM particles are selected to have a diameter of 2 µm.

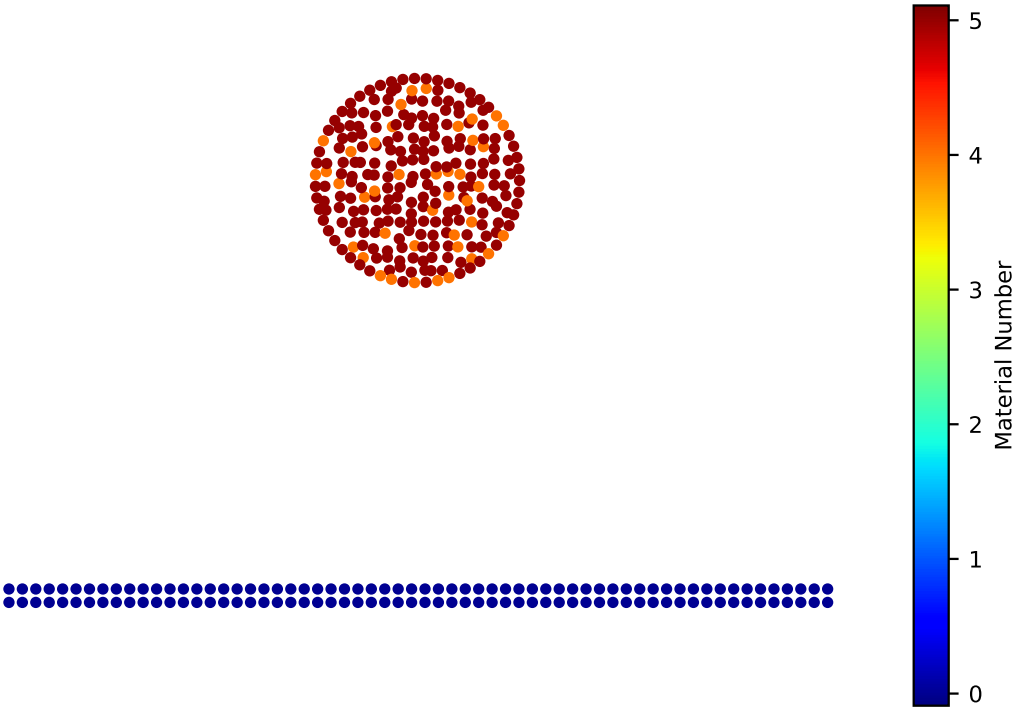

Figure 4.1: Initial position of particles for single droplet impact for test case 8 in table 4.4. Material numbers correspond to the wall, 0 or dark blue, photopolymer, 5 or red, and additive, 4 or orange.

With the sizes selected, the next step is to create the particle domain. The initial position of the center of the droplet is selected to be 70 μm above the build surface. This provides sufficient distance between the droplet and surface so that they do not begin in contact while not wasting computational time on moving the droplet with no drag through the ambient environment. Next the outer boundary of the droplet is created by generating a spherical, or circular, boundary centered about the initial position. Since the droplet motion through the ambient environment is neglected, the spherical boundary reduces the effects of artificial surface tension resulting from initial particle positions. After the boundary is defined, the interior of the domain is generated by randomly placing particles within the domain ensuring that a minimum spacing is maintained between any two points. The final step is to generate the impact surface. To create a smooth surface, particles are placed a uniform distance apart in a perfect grid with a width equal to four times the diameter of the droplet.

The last consideration is that in each test case the particles must start in the same position. This is necessary since changing the starting position without changing any of the material properties or process parameters will result in small but measurable difference in the resulting droplet shape. Thus to generate different input files, all but the material number identifying the material type remains unchanged. The number of particles assigned with an additive material number is selected to correspond to the desired test weight fraction.

4.2.2 Results

Figure 4.2 illustrates the impact response and temperature of a single droplet with an additive weight fraction of 0.2 and Figure 4.3 illustrates the final deposition shape and temparature for each of the eight test cases after 0.15 ms. The response of the material is as expected in that the single droplet spreads across the build surface before surface tension pulls the material back toward the center of the domain resulting in a single domed droplet. The cooler region on the bottom right edge of the domain corresponds to a higher concentration of additives in a single area. This higher concentration results in a more rapid cooling due to the difference in thermal conductivity between the additives and the photopolymer resin.

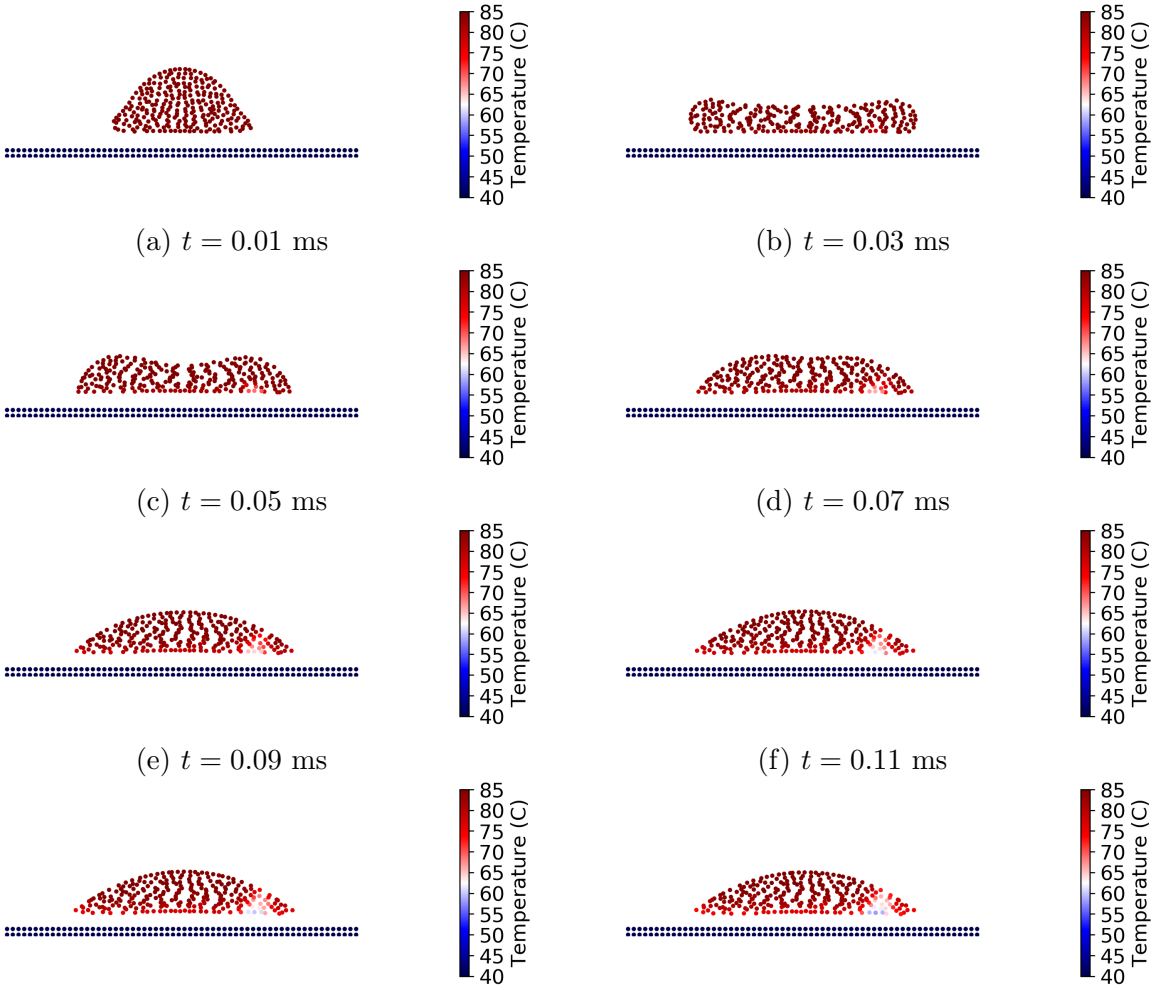

(a) $t = 0.01$ ms (b) $t = 0.03$ ms

(c) $t = 0.05$ ms (d) $t = 0.07$ ms

(e) $t = 0.09$ ms (f) $t = 0.11$ ms

(g) $t = 0.13$ ms (h) $t = 0.15$ ms

Figure 4.2: The results of a single droplet impacting the build surface at eight time steps starting at $t = 0.01$ ms and ending at $t = 0.15$ ms for test case 7 in Table 4.4.

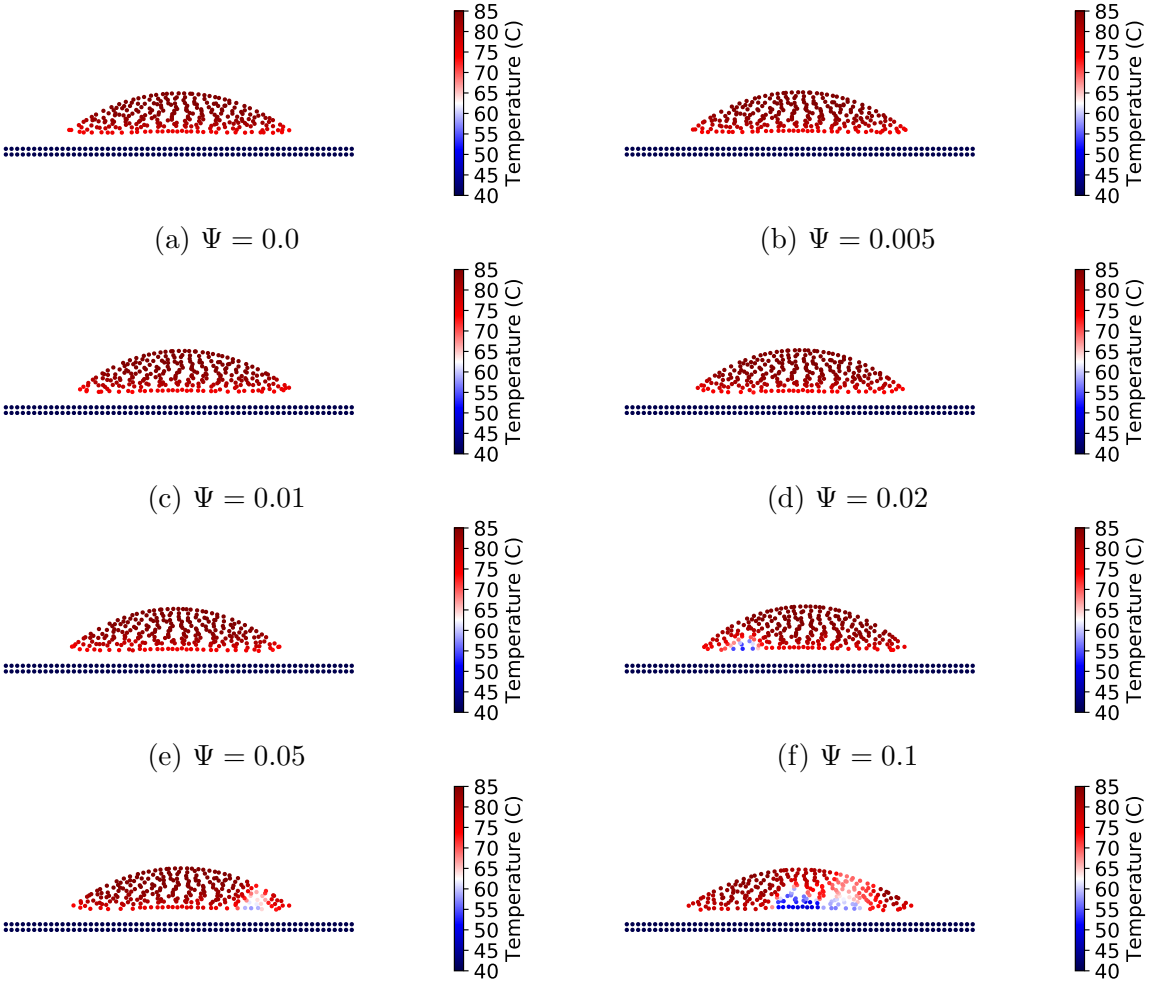

(a) $\Psi = 0.0$ (b) $\Psi = 0.005$

(c) $\Psi = 0.01$ (d) $\Psi = 0.02$

(e) $\Psi = 0.05$ (f) $\Psi = 0.1$

(g) $\Psi = 0.2$ (h) $\Psi = 0.5$

Figure 4.3: Shape and temperature of a single droplet after 0.15 ms for all eight test cases.

To compare the results of each of the resulting impacts, the width, maximum height, and average height of each droplet are considered. Each of these measurements are idenfitied by first isolating the particles defining the top boundary of the droplet. Using these particles the width is determined by taking the difference between the extreme x-values, the maximum height is taken as the maximum y-value, and the average height is taken as the average of all the y-values. Each of these values for the eight test cases are shown in Figure 4.4.

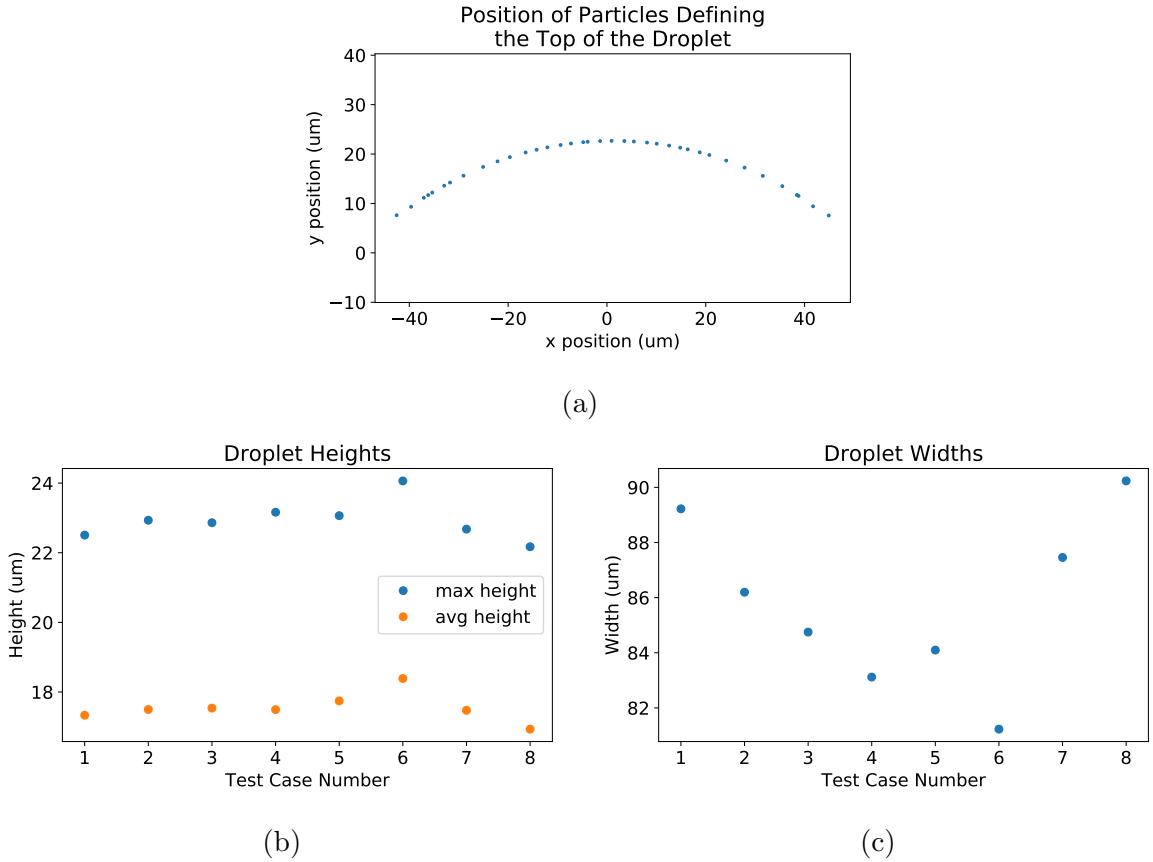

(a)

(b)

(c)

Figure 4.4: The (a) surface profile for test case 7, a weight fraction of 0.2., (b) maximum and average height of the droplet for each test case after 0.15 ms, and (c) width of the droplet for each test case after 0.15 ms.

As the weight fraction of additives increases to 0.1, the height of the droplet increases and the width decreases indicating that the droplet spreads less upon impact. Once the weight fraction exceeds this value, the increased density of the droplet results in a return to the spreading behavior with the greatest weight fraction, 0.5, producing a droplet that spreads more than the pure photopolymer resin.

The extent of the decrease in spreading from the pure photopolymer resin, test case 1, to the composite containing a weight fraction of 0.2, test case 6, is 8.0 μm. The change in the height is less significant with the max height increasing by 1.6 μm and the average

height increasing by 1.1 μm. These changes influence the layer formation process in that the decreased droplet width requires that the droplets be placed closer together so that they may merge producing a smooth and stable print line. The increase in droplet height in combination with the droplets being placed closer together has the effect of increasing the print line height. As the height increases, the material takes longer to cure due to reduced light penetration at the bottom of the layer. Alternatively, a taller layer can result in more wasted material if a planarization step is utilized to decrease the height to the desired thickness.

4.3 Degree of Cure Study

4.3.1 Overview of Objectives and Methodology

To isolate the impacts of additives on the degree of cure within the material, the system of choice to model is a stereolithography (SLA) type process in which a large volume of material is exposed to a laser light source. By eliminating the layering process of inkjet printing we can look at how far and how fast the curing front propagates into the material. Understanding the curing response of the material provides fundamental knowledge that is utilized to develop a characterization tool for the inkjet printing process.

In addition to considering the weight fraction of additives, we also consider the effects of the peak light intensity with two sets of process parameters. The first set is a light intensity of 25 mW/cm^2 with an exposure time of 2 seconds. The peak intensity of 25 mW/cm^2 is selected for the first set since most inkjet printers utilize a light source with a peak intensity between 20 and 30 mW/cm^2 [34]. The second set is a light intensity of 2.5 mW/cm^2 with an exposure time of 20 seconds. This peak intensity is outside of the typical process design range but the exaggerated difference highlights the influence of the light intensity while exposure for 20 seconds ensures the same total energy applied to the top surface. For both light intensities, eight weight fractions are tested, Table 4.5.

Table 4.5: Test cases for effects of additives on the photopolymer curing response.

Test Case	1	2	3	4	5	6	7	8
Weight Fraction	0.0	0.005	0.01	0.02	0.05	0.1	0.2	0.5

One of the input files for the degree of cure study is shown in Figure 4.5. The input file is generated by placing all of the particles in regular grid and then are held fixed for all time. This eliminates the impact of particle positions and movement from the curing behavior. The material number of each particle is then assigned randomly such that the number of additive particles corresponds to the desired test weight fractions.

While the inkjet printing process has layer thicknesses of 14 to 32 μm [53, 55] the domain is selected to be 480 μm deep with a width of 32 μm. This allows for a more comprehensive overview of the changes in the curing response due to additives.

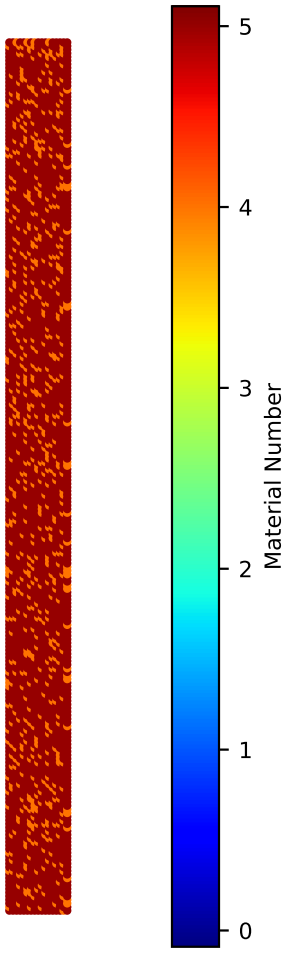

Figure 4.5: Position of particles in degree of cure study for test case 8 in table 4.5. Material numbers correspond to the wall, 0 or dark blue, photopolymer, 5 or red, and additive, 4 or orange.

4.3.2 Results

The degree of cure over time for a material containing a 0.2 weight fraction of additives exposed to a light source with peak intensity of 25 mW/cm^2 is shown in Figure 4.6. The results show how the dispersion of additives can impact the degree of cure. This is most noteable in Figures 4.6d and 4.6e, in which the curing profile has a nonuniform shape. The nonuniformity in the degree of cure results from photopolymer particles directly below additive particles being exposed to a lower light intensity and thus have a lower degree of cure.

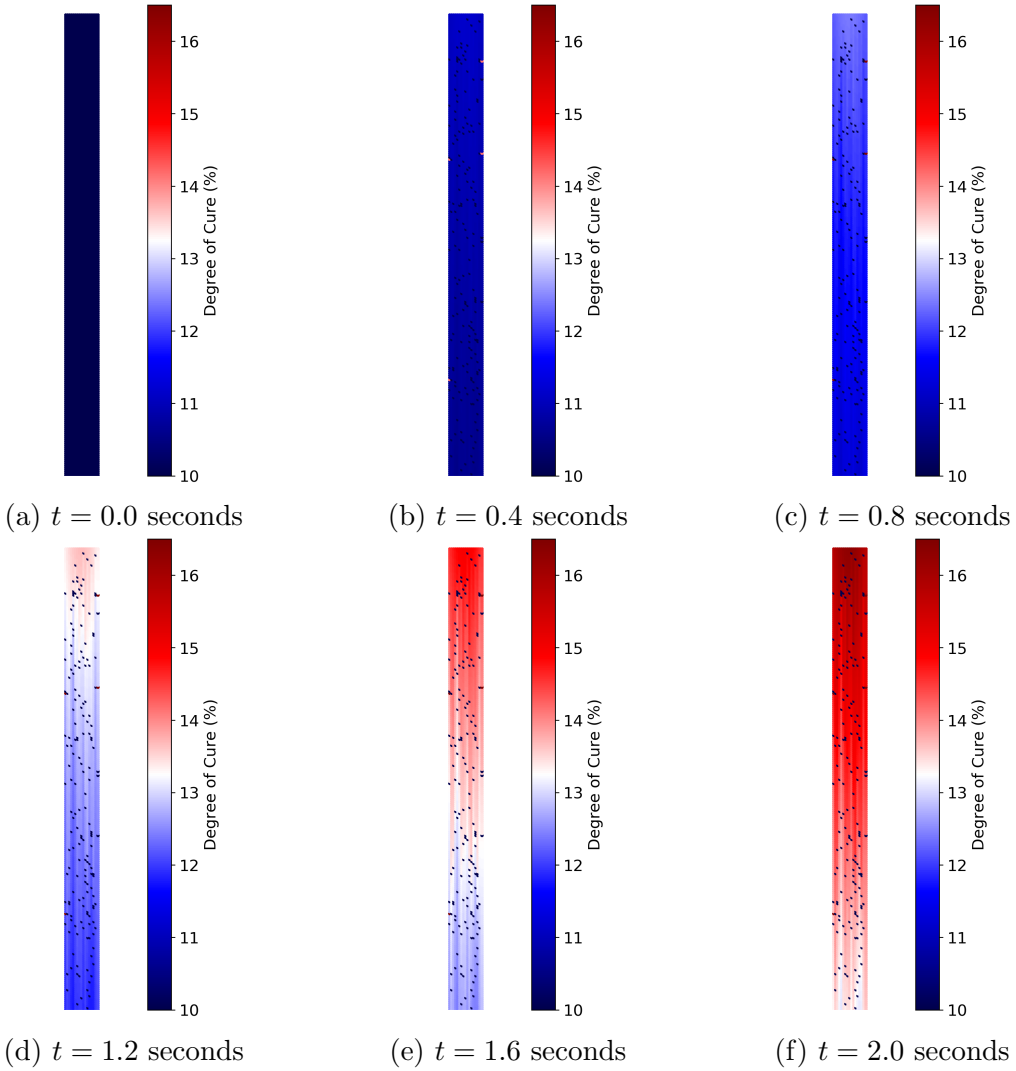

(a) $t = 0.0$ seconds (b) $t = 0.4$ seconds (c) $t = 0.8$ seconds

(d) $t = 1.2$ seconds (e) $t = 1.6$ seconds (f) $t = 2.0$ seconds

Figure 4.6: The degree of cure at six time steps starting at time $t = 0$ and ending at $t = 2$ second for a weight fraction of 0.2 exposed to a light source with a peak intensity of 25 mW/cm^2.

The final degree of cure profiles for all eight test cases after exposure to the 25 mW/cm^2 light source are shown in Figure 4.7. From the final profiles, the decrease in the degree of cure deeper into the material as a result the increase in weight fraction of additives is clearly seen. Upon visual inspection, low weight fraction of additives, 0.005 to 0.02, have an almost negligible effect except at the farthest points from the light source. The mid weight fraction, 0.05 to 0.2, produce a more pronounced effect with degree of cure at the deepest point being clearly reduced. The final case in which the weight fraction is 0.5, the decrease in the degree of cure is substantial enough that it is possible this high a weight fraction would be unusable for this type of curing process.

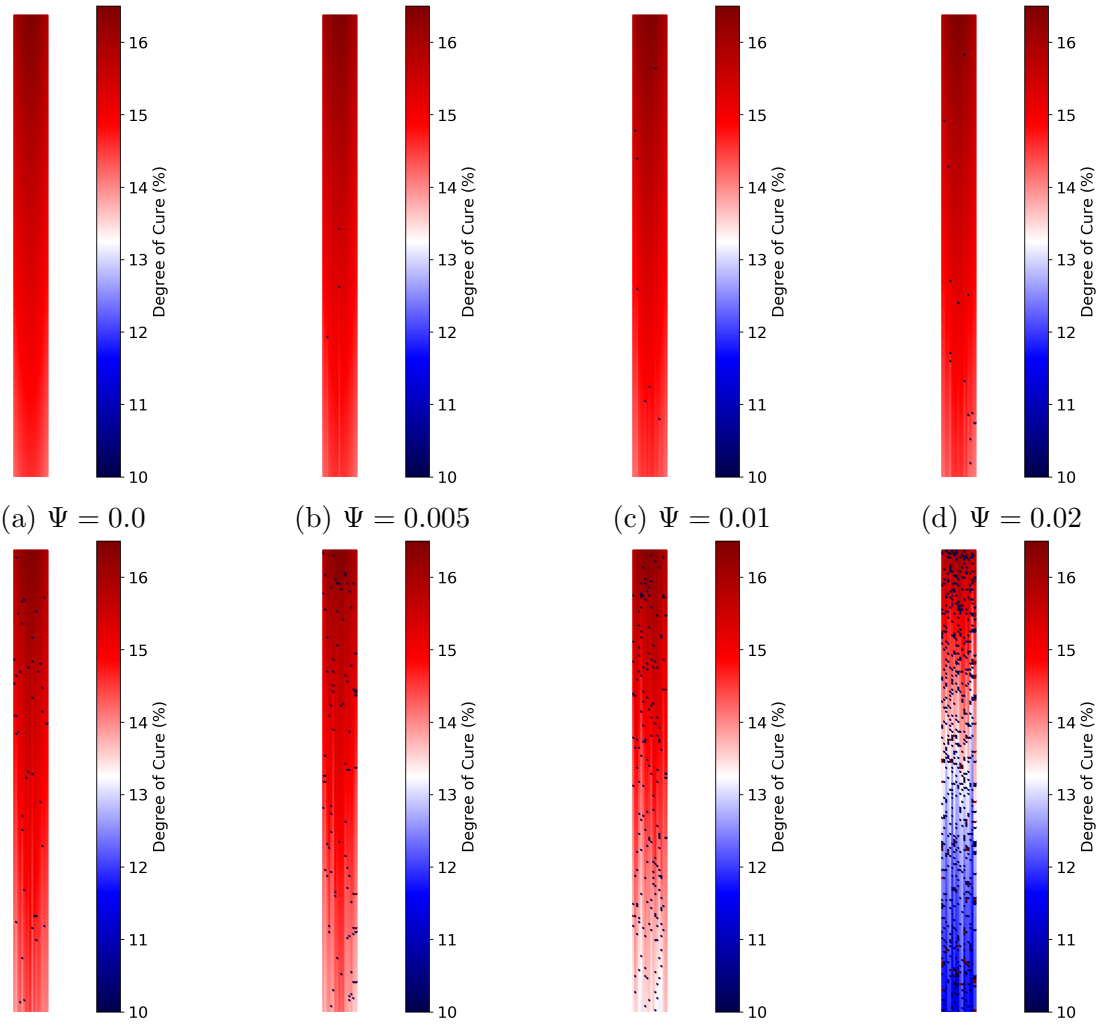

(a) $\Psi = 0.0$ (b) $\Psi = 0.005$ (c) $\Psi = 0.01$ (d) $\Psi = 0.02$

(e) $\Psi = 0.05$ (f) $\Psi = 0.1$ (g) $\Psi = 0.2$ (h) $\Psi = 0.5$

Figure 4.7: Final degree of cure profiles for all eight test cases exposed to 25 mW/cm^2 after 2 second.

To better characterize the effects of the additives, the average degree of cure of the photopolymer is calculated at each depth, Figure 4.8. For both plots, the observations made previously with the final degrees of cure profiles are more clearly demonstrated. At low weight fractions, less than 0.05, there is an almost negligible change in the degree of cure with depth. The mid weight fractions, up to 0.2, start to have a noticable departure from the pure photopolymer case with a greater difference deeper into the material. The increased difference deeper into the material is a direct result of the decrease in light penetration. When producing a large part, the reduction in light penetration must be considered since the final overall degree of cure through the material may be lower than desired or may over time become unevenly cured while in use.

For the final weight fraction of 0.5, the additives make the material difficult to cure resulting in a greater overall decrease in the degree of cure. Most notibly there is a large decrease in the degree of cure on the top surface. This is likely due to the additives decreasing the ability for monomer to diffuse toward the top surface; less monomer means a slower propagation rate and thus a lower degree of cure. While the decrease in the degree of cure on the top surface can be accounted for through changing process parameters to increase exposure time, the concerns of an under cured final part are greater than in the case of a composite with fewer additives.

The most noticeable difference between the two sets of simulations is the final degree of cure differs by a factor of approximately four, relative to the starting degree of cure of 10%, even though they have been exposed to the same total energy. This behavior is expected due to the necessity to expose the materials to varying lengths of time to reach the same total energy. Specifically, the longer the exposure time, the longer the polymerization process continues even if the active chain concentration is lower.

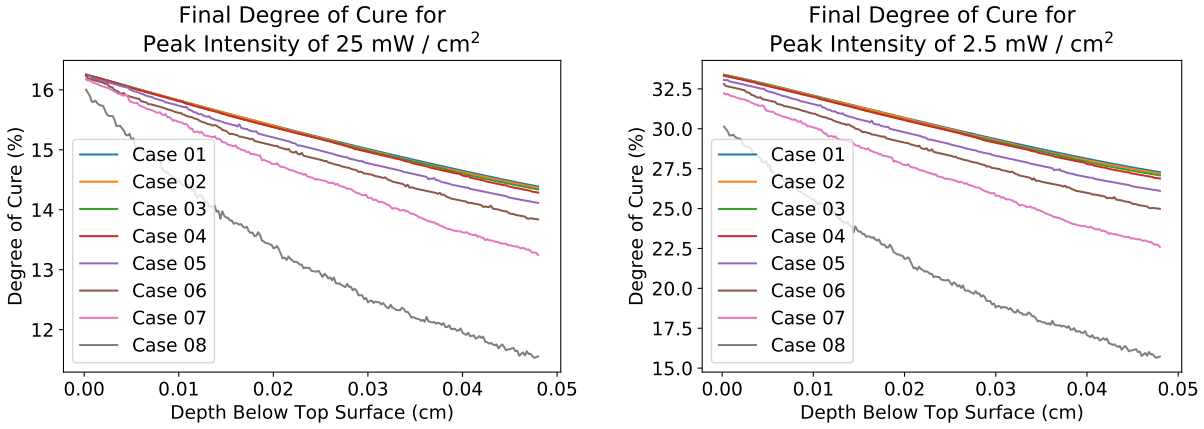

(a) (b)

Figure 4.8: Average degree of cure through the material after applying 50 mJ/cm^2 of energy to the top surface given a peak light intensity of (a) 25 mW/cm^2 and (b) 2.5 mW/cm^2.

To better understand the effects of additives for the propose of characterizing the curing response during a layer by layer deposition and curing process, the time data it utilized to track the solidification front corresponding to the gel point as it penetrates into the material. The solidification front provides insight into when the material transitions from the liquid resin into a gel material that is capable of retaining its shape as new material is being deposited. For this work, the degree of cure corresponding to the gel point is selected to be 15%; this is the minimum of the experimental values for HEMA, 15 to 20% [35].

The results of tracking the depth of the solidification front versus exposure time are shown in Figure 4.9. While the previous plots illustrated that the lower intensity with greater exposure time resulted in greater degree of cure, these figures demonstrate that the higher intensity results in a faster curing rate as evident by the solidification front starting more than 3.5 seconds earlier than the lower intensity case. The faster curing rate comes from the higher intensity converting more of the photoinitiators into active chains and thus consuming monomer at a faster rate. This is beneficial for the printing process as it allows for faster deposition of material and thus faster overall part production.

More importantly, these figures demonstrate that increasing weight fraction of additives results in a slower solidification front propagation rate even though the top of the domain reaches the gel point at approximately the same time. This is most evident in Figure 4.9b as the solidification fronts reach the bottom of the computational domain at later and later times with an increasing weight fraction of additives. The slower propagation rate means that the layer requires more time to cure which results in the top surface reaching a greater degree of cure creating a larger difference at the interface between two layers. Recall that this difference is important since a larger difference in the degree of cure corresponds to a larger difference in the percentage of shrinkage resulting in internal stresses that cause parts to curl or warp. Additionally, the longer it takes before the next layer can be deposited the longer it takes to produce the final part.

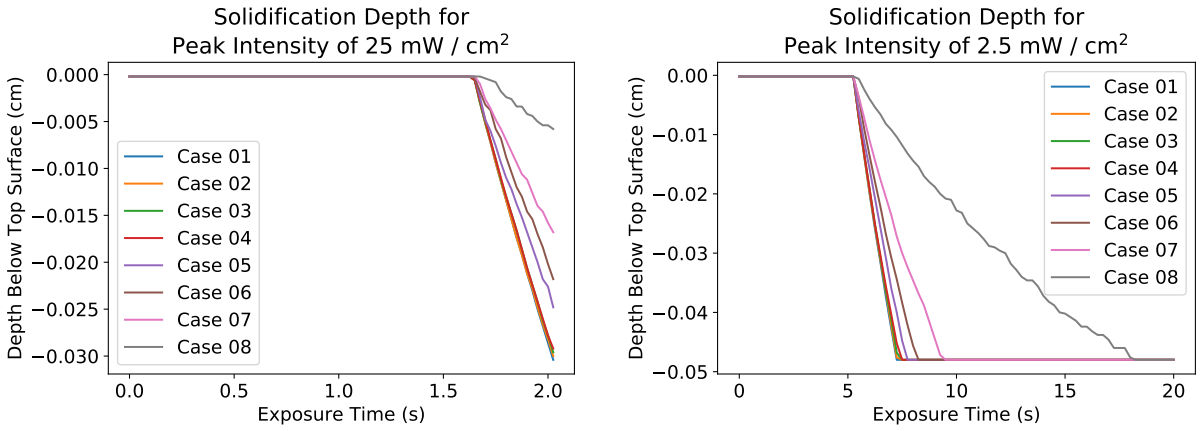

(a) (b)

Figure 4.9: Depth into the material that has been solidified versus the exposure time to a light source with peak intensity of (a) 25 mW/cm^2 and (b) 2.5 mW/cm^2.

4.4 Conclusions

Some of the key observations made from each model regarding the effect of additives on the thermo-mechano-chemical reponse of a material utilized in inkjet printing are as follows. From the single droplet impact, it is observed that the weight fraction of additives effects the final width and height of the droplet after deposition. The decreased width observed at the low and mid weight fraction of additives results in droplets needing to be placed closer together in order to prevent gaps or thin regions within a layer from forming.

Any buldging or gapping that may form from droplets being placed either too far or too close together can be negated by introducing a roller system that can smooth out the layers. The inclusion of additives possess a challenge to this solution in that they become abrasives that over time scratch or adhere to the roller decreasing its ability to level the material. This means that it is still desirable to produce even layers with limited dependence on a roller.

The degree of cure models demonstrate that the increase in additives decreases the degree of cure into the material. The decrease in the cure deeper into the material illustrates the importance of tracking the overall degree of cure at the end of the build since if the polymerization rate slows too much a part with a large volume can be undercured or result in nonuniform degree of cure. The decrease also leads to the necessity to allow for longer curing times between layer deposition which can result in a final part with a greater likelihood of curling or warping. Thus it is important to understand how long it takes for the entire layer to reach the gel point and to what extent the top of the layer has cured.

Chapter 5

Modeling of Inkjet Printing System

5.1 Modeling Overview

To study the effects process parameters have on the response of an additive-polymeric composite fluid, the inkjet printing process is initially considered in two parts. The first model is limited to the thermal and mechanical response of the material prior to curing. This is done with a model composed of multiple droplets deposited onto a build surface, which allows us to focus on the deposition response in determining the optimal process parameters. The second model studies the curing behavior of multiple layers without considering the mechanical response. This model provides information on the solidification behavior between layers at a reduced computational expense.

To characterize the results of each of these studies, the final response is utilized to develop a objective function. The objective function provides an algorithmic method for characterizing how well the results of the models match the desired outcome. The general form of an objective function is given as

$$\Pi = \sum_i w_i \left| \frac{x_i}{x_i^D} - 1 \right|^2 \tag{5.1}$$

where Π is the numeric value of the objective function, w_i is the weight for the desired parameter, x_i is a measurable variable from the model, and x_i^D is the desired value for the measurable variable.

The material properties and inital concentrations for both of these studies are the same as those used in Chapter 4, Tables 5.1 and 5.2. The initial degree of cure is maintained to be 10% and to ensure a noticable effect of the additives on the process parameters the composite is composed of 0.2 weight fraction of additives, approximately corresponding to a volume fraction of 0.046.

Table 5.1: Comprehensive list of material constants for inkjet printing models.

Parameter	Symbol	Value	Units
Volume fraction, additive	Φ_a	0.046	
Density, additive	ρ_a	5820	kg / m^3
Density, initiator	ρ_s	1132	kg / m^3
Density, monomer	ρ_m	1073	kg / m^3
Density, polymer	ρ_p	1150	kg / m^3
Reference viscosity	μ_0	1.720×10^{-6}	Pa·s
Activiation energy, thermal	E_θ	26200	
Surface tension	γ	0.0485	N / m
Thermal conductivity	$\mathbb{K}$	0.2	W / m·K
Heat of polymerization	ΔH_p	54.8×10^3	W / mol
Heat capacity	c	1700	J / kg·K
Diffusion constant pre-exponential, monomer	$D_{m,0}$	2.36×10^{-6}	m^2 / s
Diffusion constant parameter, monomer	A_m	0.66	
Initiator absorptivity	ϵ_s	15×10^3	L / mol·m
Additive absorptivity	ϵ_a	9.15×10^2	L / mol·m
Quantum yield of initiation	ϕ	0.6	
Coefficient of thermal expansion, monomer	α_m	0.0005	1 / K
Coefficient of thermal expansion, polymer	α_p	0.000075	1 / K
Glass transition temperature, monomer	$\theta_{g,m}$	213	K
Glass transition temperature, polumer	$\theta_{g,p}$	328	K
True kinetic constant, polymerization	k_{p0}	1.6×10^6	L / mol·s
Activation energy, polymerization	E_p	18.23×10^3	J / mol
Diffusion parameter, polymerization	A_{Dp}	0.66	
Critical free volume, polymerization	f_{cp}	0.042	
True kinetic constant, termination	k_{t0}	3.6×10^6	L / mol·s
Activation energy, termination	E_t	2.94×10^3	J / mol
Diffusion parameter, termination	A_{Dt}	1.2	
Critical free volume, termination	f_{ct}	0.060	
Reaction diffusion parameter	R_{rd}	4	

Table 5.2: List initial concentrations for the photopolymer and additive particles.

Parameter	Symbol	Value	Units
Monomer concentration	$[M]$	8.2	mol / L
Active chain concentration	$[M\cdot]$	0.0	mol / L
Photoinitiator concentration	$[S]$	0.1	mol / L
Additive concentration	$[A]$	30.4	mol / L

5.2 Multiple Droplet Layer Formation Study

5.2.1 Overview of Objectives and Methodology

In the single droplet impact study, it was observed that the width and height of each droplet changed as the weight fraction changed. While interesting, this does not inform the process parameters necessary for producing relatively smooth and stable print lines. Thus the objective of this study is to look at how ejection velocity, scanning velocity, and droplet release frequency impact the ability to produce the desired print lines for inkjet printing.

Each of the three process variables are considered for the following reasons. The ejection velocity is considered since it controls the shape of a single droplet and thus the behavior of droplets as they merge. At low ejection velocities, the droplets have the least amount of spreading and require closer placement between sequencial droplets and greater dependence on surface tension to cause droplet merging. As the ejection velocity begins to increase the droplets prefer to spread upon impact due to having greater momentum. The ejection velocities selected for this study originate from a range of experimentally achievable values, 4 to 9 m/s, observed by Khalate et al. [31].

The scanning velocity of the print head is considered since the faster the print head passes over the build surface the faster the part can be built, but the faster the print head is moving and the more horizontal momentum each droplet contains. This momentum leads to challenges with controlling where droplets land and how it spreads. The range of velocities for the print head are limited to be 0.3 and 0.9 m/s. These velocities are chosen since a common dimension for the printable range of a build platform is approximately 12 inches or 30 cm [53, 55]. Velocities of 0.3 and 0.9 m/s means that the print head is capable of covering the printable area in 1 to 0.33 seconds.

The final parameter is the droplet release frequency. The release frequency is considered since in combination with the scanning velocity, this parameter controls the spacing between released droplets. If the frequency is too low relative to the print head velocity, droplets will be produced too far apart producing individual droplets rather than a single line. On the other hand, if the frequency is too high relative to the print head velocity, droplets will overlap to an extent that the lines become unstable and begin to bulge.

For the purposes of developing an objective function to characterize the line formation, the center to center droplet spacings are specified in place of a release frequency. This is necessary to ensure that the objective function is sensitive enough to capture the subtle but observable differences between two results. For this reason, the range of spacinges are 80.5 to 84.0 μm. Calculating the release frequency from the velocity and spacing results in frequecies bounded between 3500 and 11000 kHz. Both of the extremes fall within the feasible range of drop-on-demand inkjet printing heads, 250 Hz to 20 kHz [11, 18].

To demonstrate the range of effects that these process parameters have, a series of model problems are run in which all variables range between the extreme values, Table 5.3.

Table 5.3: Table of test cases for a multiple droplet deposition for layer formation study.

Test Case		1	2	3	4	5	6	7	8
Ejection Velocity	[m/s]	5	5	5	5	8	8	8	8
Scanning Velocity	[m/s]	0.3	0.3	0.9	0.9	0.3	0.3	0.9	0.9
Release Spacing	[µm]	80.5	84.0	80.5	84.0	80.5	84.0	80.5	84.0

The input file for the layer formulation study is generated by following a similar process to the single droplet study. Four droplets are created with a diameter of 35 µm, the particles have a diameter of 2 µm, and each containing a number of additive particles corresponding to a weight fraction of $\Psi_a = 0.2$. To minimize the impact of particle placement, the first droplet released in all cases has the particles placed in the same configuration. The second droplet has a different particle configuration than the first but are the same across all cases; this is true for all four droplets. To generate each set of input files, a single droplet is created then the initial position and velocity are modified to the approriate test case.

Figure 5.1 shows the starting positions of the droplets in test case 1. Initially, droplet farthest on the left in imported and the simulation begins. The next droplet is imported at the time step corresponding to the release frequency. This process repeats for the remaining two droplets before the simulation terminates.

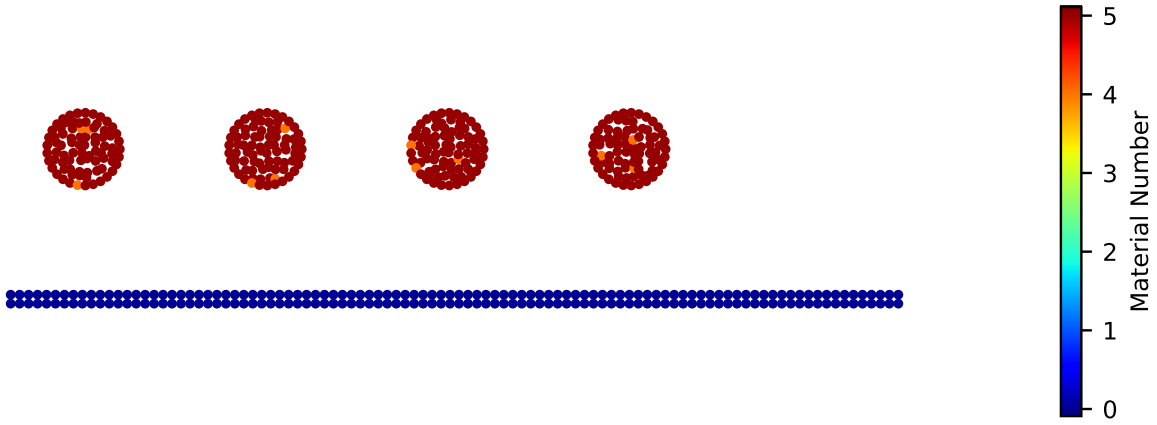

Figure 5.1: Position of particles in the layer formation study for test case 1 in Table 5.3. While the initial position of each droplet is illustrated in this figure, each droplet is introduced into the model at a specific time step corresponding to the test case release frequency proceeding from left to right. Material numbers correspond to the wall, 0 or dark blue, photopolymer, 5 or red, and additive, 4 or orange.

5.2.2 Results

The deposition of four droplets onto a build surface for test case eight are shown in Figure 5.2. The results show the first droplet behaves as expected from the single droplet study. The second droplet impacts and spreads, but due its momentum and the surface tension between the two droplets they merge creating a lower overall profile where the second droplet landed. The third droplet splashes upon impact, evident by the material at the far right of Figure 5.2f. The splashing results in material being pushed further into the second droplet than might be anticipated and the surface tension pulls the material back on the right creating a small area of increased volume. The fourth droplet spreads without splashing and again material is pulled to the left toward previously deposited material. From the thin regions on either side of the third droplet that are appearing, if the process were to continue regions of less material may appear indicating that the droplet spacing is too far apart.

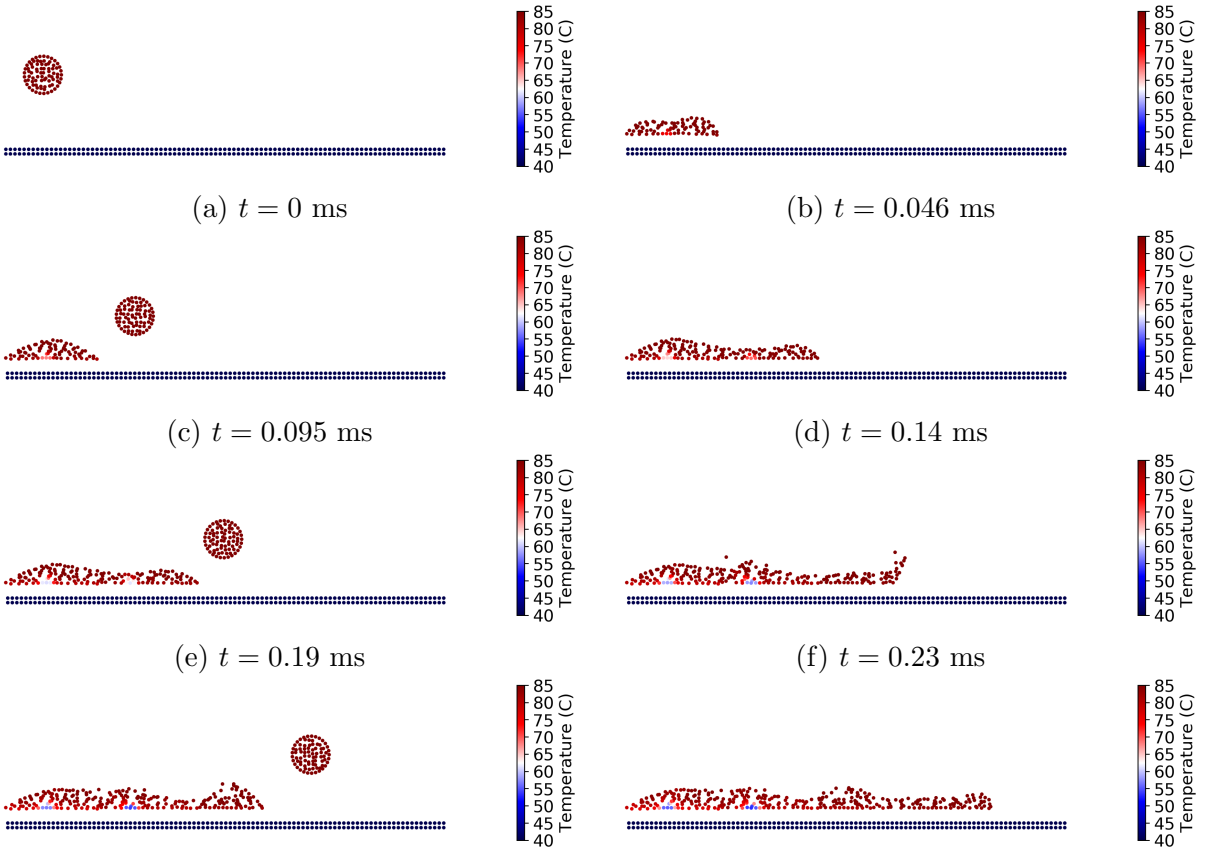

(a) $t = 0$ ms (b) $t = 0.046$ ms

(c) $t = 0.095$ ms (d) $t = 0.14$ ms

(e) $t = 0.19$ ms (f) $t = 0.23$ ms

(g) $t = 0.28$ ms (h) $t = 0.33$ ms

Figure 5.2: Deposition of four droplets onto the build surface at eigth time steps starting at $t = 0$ and ending at $t = 0.33$ ms for test case 8: ejection velocity, v_e, of 8 m/s, scanning velocity, v_s, of 0.9 m/s, and release spacing, ds, of 84 µm.

The final time step for all eight test cases are shown in Figure 5.3. Several important observations can be made. First, the slower scan velocity of test cases 1, 2, 5, and 6 results in the material having a greater period of time to cool. In combination with the material curing, the lower temperature results in a higher viscosity making the layer more resilient to deformation during the depositon of the next layer. If a planarization step is necessary, the increase viscosity also makes the material more resistent to flowing.

Second, the release spacing and thus frequency illustrates the sensitivity of the material to the impact locations. Most evident in test cases 1 and 2, the increase in droplet spacing prevented the second and third droplet from properly merging leaving a small region with almost no material. This region can be filled with the use of a roller, but if the height of the layer is already too low, there may be insufficient material to fill the gap.

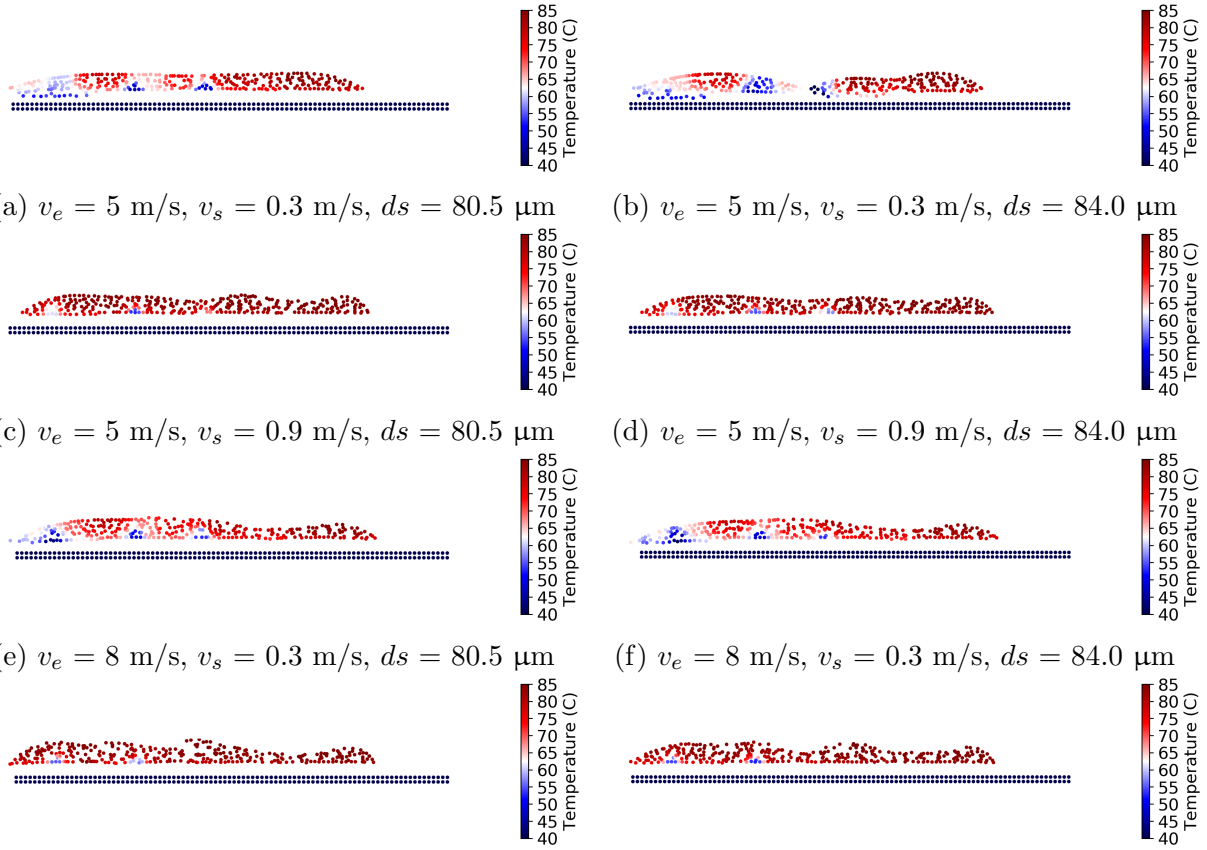

(a) $v_e = 5$ m/s, $v_s = 0.3$ m/s, $ds = 80.5$ µm (b) $v_e = 5$ m/s, $v_s = 0.3$ m/s, $ds = 84.0$ µm

(c) $v_e = 5$ m/s, $v_s = 0.9$ m/s, $ds = 80.5$ µm (d) $v_e = 5$ m/s, $v_s = 0.9$ m/s, $ds = 84.0$ µm

(e) $v_e = 8$ m/s, $v_s = 0.3$ m/s, $ds = 80.5$ µm (f) $v_e = 8$ m/s, $v_s = 0.3$ m/s, $ds = 84.0$ µm

(g) $v_e = 8$ m/s, $v_s = 0.9$ m/s, $ds = 80.5$ µm (h) $v_e = 8$ m/s, $v_s = 0.9$ m/s, $ds = 84.0$ µm

Figure 5.3: Final position and temperature of four 35 µm diameter droplets at various ejection velocity, v_e, scanning velocity, v_s, and release spacing, ds; test cases are listed in Table 5.3. for all eight test cases, Table 5.3.

Finally, the increased ejection velocity results in greater spreading of the material which can eliminate some of the problems of droplets being placed too far apart. This can be seen by comparing test case 2 and 6, Figures 5.3b and 5.3f respectively. The gap initially formed between droplets two and three in case 2 is eliminated in case 6.

Alternatively, the increased ejection velocity can result in the formation of a thin region when none was present before, test cases 1 and 5, Figures 5.3a and 5.3e respectively. These two countering results in which only the ejection velocity changed highlights some of the complexity in determing the desired process parameters.

While the above insights are useful for understanding the importance of process parameters, to develop our objective function the final profiles must be simplified to measurable values. This is done by first extracting the particles defining the top surface. Using these particles, we calculate the length, maximum height, average height, and standard deviation of the surface profile from the average value, Figure 5.4.

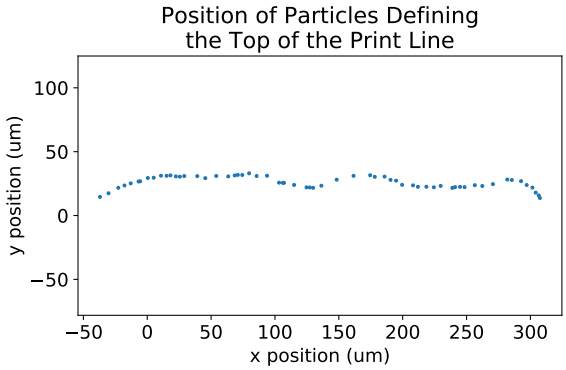

(a)

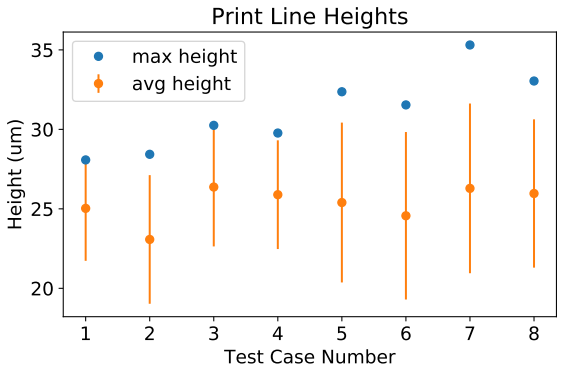

(b)

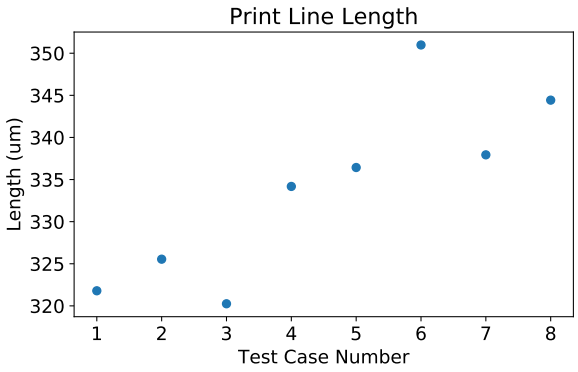

(c)

Figure 5.4: The (a) surface profile for test case 8, (b) maximum and average height with standard deviation, and (c) length of the final profiles.

The height information provides the most insight into how well the process parameters perform. From visual inspection of the final profiles test cases 1 and 4 appear to be the best performing while test cases 7 and 8 are the worst performing. These observations are captured in the height measurements by the different in the maximimum and average heights and the standard deviation in the heights. For test cases 7 and 8 the difference between the maximum and average is 9.0 and 7.0 μm with a standard deviation of 5.3 and 4.7 μm, respectively. In contrast, test cases 1 and 4 have a difference of 3.0 and 3.9 μm with a standard deviation of 3.3 and 3.4 μm, respectively.

From the print line length information, it is clear that lower ejection velocities, cases 1 through 4, produce shorter print lines on average. Additionally, increased spacing between droplets, test cases 2, 4, 6, and 8, produce longer print lines than the closer spaced counter parts. Neither of these observations are unexpected. Interestingly, no trend is observed related to the scanning velocity as test cases 3, 4, 7, and 8 did not always result in longer print lines. This is likely due to the effects of surface tension and any resulting droplet splashing.

While a clear correlation between how well the process parameters produce a stable line can be seen in the height data, no such correlation exists with the length. Thus the print line length is not necessary in the determination of optimal process parameters.

5.2.3 Objective Function Development

Starting with the general form of the objective form and measurable values of maximum, average, and standard deviation of the height, the general form for layer formation in inkjet printing is

$$\Pi = w_1 \left| \frac{h_{avg}}{h^D_{avg}} - 1 \right|^2 + w_2 \left| \frac{h_{stdev}}{h^D_{stdev}} - 1 \right|^2 + w_3 \left| \frac{h_{max}}{h^D_{max}} - 1 \right|^2 \tag{5.2}$$

where w_i for $i = 1, 2, 3$ are the weight for each term and h^D_j for $j = max, avg, stdev$ are the desired height terms.

The average layer height is included since the objective is to produce a layer thickness as close to the desired thickness as possible. To align with the desired print thicknesses often employed in inkjet printers, the desired average layer height, h^D_{avg} is set to 16 μm. In an ideal scenario, the variation in the layer thickness is zero but for the purposes of the objective function, the standard deviation from the average height, h^D_{stdev}, is limited to 1 μm. Finally, a surface that is relatively smooth with small but sharp peaks should be considered to perform worse and thus the maximum height is included. To prevent the peaks from becoming too large the maximum height, h^D_{max}, is limited to be within one standard deviations of the average, given the prior parameters, the maximum height is limited to $h_{avg} + 1$ μm.

Since the desired value for the standard deviation and maximum height are limits rather than specifically desired values, the weight for each variable can be applied with a heaviside step fuction. In both cases, the weight should be nonzero when the current value is greater

than the desired value. The resulting weights are thus

$$w_2 = w_2 H(h_{stdev} - h^D_{stdev}) \quad \text{and} \quad w_3 = w_3 H(h_{max} - h^D_{max}) \tag{5.3}$$

where $H(x)$ is the heaviside step function. Finally, the specific values of each weight are selected such that the average value has a weight two times the other two parameters. This is done since the standard deviation and maximum height capture similar responses; specifically, the standard deviation focuses on the variation over the entire profile while the maximum focuses on the variation of a single peak. For simplicity, the final value for the nonzero weights are

$$w_1 = 1.0 \quad w_2 = 0.5 \quad w_3 = 0.5 \tag{5.4}$$

Plugging the parameters into the general objective function results in

$$\begin{aligned} \Pi =& 1.0 \left| \frac{h_{avg}}{16.0} - 1 \right|^2 \\ &+ 0.5 H(h_{stdev} - 1.0) \left| \frac{h_{stdev}}{1.0} - 1 \right|^2 \\ &+ 0.5 H(h_{max} - h_{avg} - 1.0) \left| \frac{h_{max}}{h_{avg} + 1} - 1 \right|^2 . \end{aligned} \tag{5.5}$$

To test the objective function for a wide range of profiles, 100 random sinusoidal profiles are generated. This is done by first creating 100 random values between -5 and 5 then adding the desired average. Next, an array of evenly spaced points is created between 0 and 4π to serve as the x-position. The y-position is generated by creating a random sinusoidal wave profile using

$$y = y_{average} + 5 * \psi_3 * (sin(x * \psi_1) + cos(x * \psi_2)) \tag{5.6}$$

where ψ_i is a new random number, x is the array of numbers between 0 and 4π, and $y_{average}$ is the randomly generated average height. The maximum and standard deviation are then calculated from the random profile. Of the randomly generated profiles the best, worst, and a mid performing are shown in Figure 5.5.

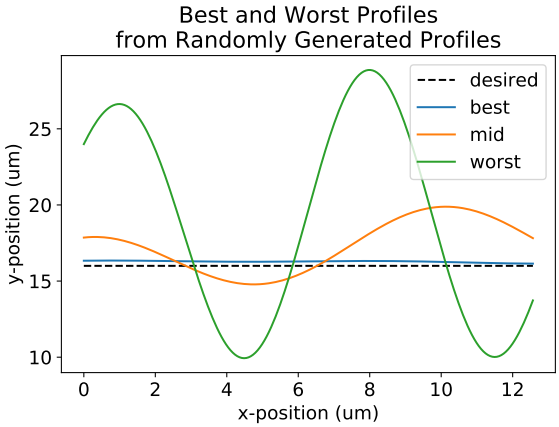

Figure 5.5: The best, worst, and a mid performer of the randomly generated surface profiles.

Results from applying the objective function to the randomly generated profiles are shown in Figure 5.6. In the first figure, 5.6a, the evaulated objective function for each randomly generated profile is sorted and plotted from minimum to maximum value. The second figure, 5.6b, shows the maximum, average, and standard deviation of each profile in the same order as the evaluated objective function.

As desired, the best performing designs have the smallest variation in profile height and have an average height near the desired value. At the other end, the worst performing designs have large standard deviations and typically an average height several micrometers off from the desired value.

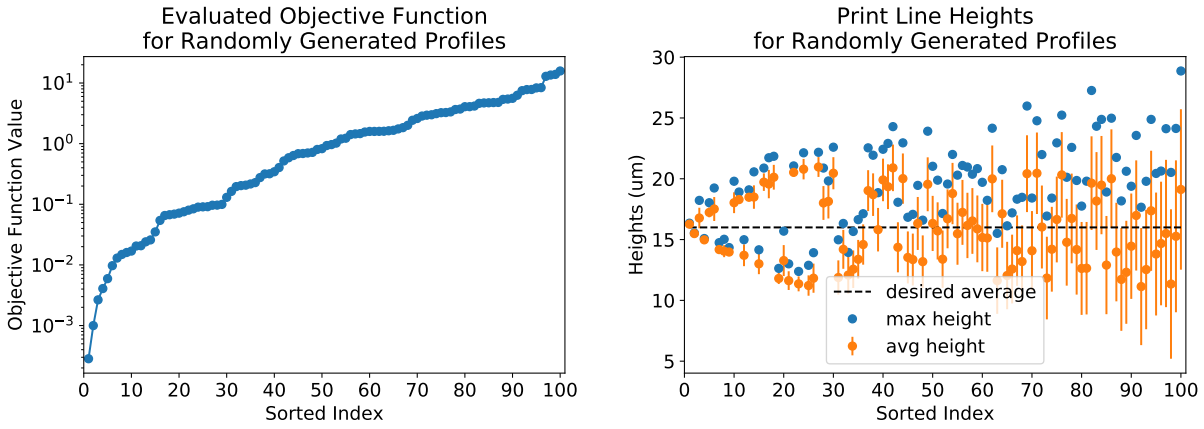

(a) (b)

Figure 5.6: The (a) evaluated objective function sorted from minimum to maximum value, best to worst performing, and (b) maximum and average height with standard deviation of the sorted randomly generated profiles.

Applying the objective function to the simulations result in the objective values shown in Figure 5.7. Based upon the visual inspection of the simulation results, the objective function is able to capture that the best performing test cases are 1 and 4 and the worst is test case 7. Additionally, the objective function clearly indicates the test cases with an ejection velocity of 5 m/s out performing all test cases with an ejection velocity of 8 m/s. This information can be used to narrow down the range of ejection velocities when performing an optimization study.

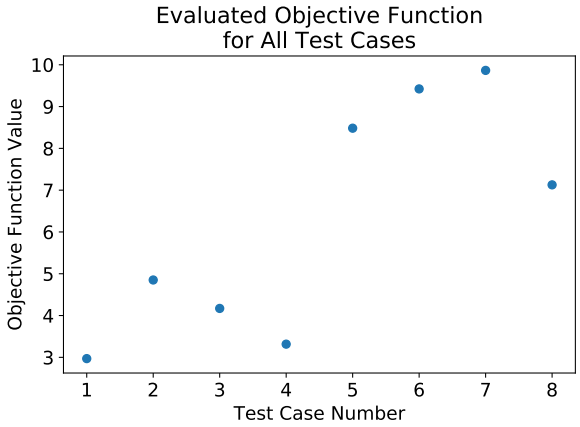

Figure 5.7: Objective function, Equation 5.5, evaluated at the final time step for all eight test cases.

5.3 Curing of Multiple Layers Study

5.3.1 Overview of Objectives and Methodology

As demonstrated by the degree of cure study as the weight fractions vary, the depth and rate to which the material cures varies. In terms of the process parameters, the peak light intensity and length of time the material is exposed to the light source also impacts curing rate. This translates to the inkjet printing process as a need to select a height and scan speed for the light source that provides the intensity and exposure time to solidify the deposited material without overcuring prior to deposition of the next layer.

The first factor is the light source height; this is selected as a control parameter since variation of the height results in a change in the area exposed to the light source at any given moment and the peak intensity on the surface of the part. The area varies with light source height since inkjet printers replace the laser light source of SLA with a series of LEDs. By using a series of LEDs, the area covered by the light source can be increased from approximately 4.9×10^{-4} cm^2 with a laser point source [20, 21] to 95 cm^2 with a single LED mounted 2 cm above the build surface [34].

To maximize coverage the height of the light source would be required to be as high as possible. Counter to this is the higher the light source the lower the peak intensity since the light must pass through the ambient environment, typically air. Typical desired peak intensity is between 20 and 30 mW/cm^2, for a UV LED source this range of desired peak intensities require the LEDs be mounted 1.8 to 2.5 cm above the top surface of the part [34]. Since longer exposure to the light source even at a lower intensity can result in a greater degree of cure, the maximum height considered for this work is 3.2 cm, a peak intensity of approximately 15 mW/cm^2.

The second factor is the scan speed since the speed at which the light source passes affects how long the material is exposed. Ideal scan speeds are as slow as possible, but the scan speed is directly impacted by droplet impact behavior of the previous study. This dependence comes from the light source being directly attached to the print heads to limit the number of independently moving components. With this limitation, the scan velocities are limited to the same range as the print head velocities, specifically 0.3 to 0.9 m/s.

To be consistent with the reasoning behind the scan velocities, the center of the light source in the x-direction varies between -10 and 20 cm. Between depositing a new layer of material the light source will pass over the material twice. It will start centered at -10 cm, pass over the material to 20 cm, then pass back over the material to -10 cm. After the two passes, another layer is added, the light source makes two passes, and the process is repeated. The entire sequence of events is repeated until three layers have been deposited and six passes of the light source are completed. The model run time for each case varies based upon the scan velocity since the number of passes and the extreme positions of the light source are fixed. The test cases and associated variables are provided in Table 5.4.

Table 5.4: Table of test cases for a simplified layered curing study.

Test Case		1	2	3	4	5	6	7	8	9
Light Source Height	cm	1.8	1.8	1.8	2.5	2.5	2.5	3.2	3.2	3.2
Light Source Velocity	m/s	0.3	0.6	0.9	0.3	0.6	0.9	0.3	0.6	0.9

The size of the domain was selected to be representative the physical process. Since the typical layer is between 14 and 32 µm depending on the machine, the layer thickness is selected to be 16 µm and the particle size is maintained at 2 µm. To maintain computational efficiency the width of the domain is limited to 100 µm. For all test cases, the particles are placed in a regular grid and held in a fixed position with each layer and the number of additive particles is determined such that the weight fraction is $\Psi_a = 0.2$.

The input files for all test cases are shown in a series of images in Figure 5.8. The first image, Figure 5.9a, is imported at the beginning of the run, while the remaining two layers are introduced after the light source as completed two passes. Figures 5.9b and 5.9c show the domain after each new layer is deposited.

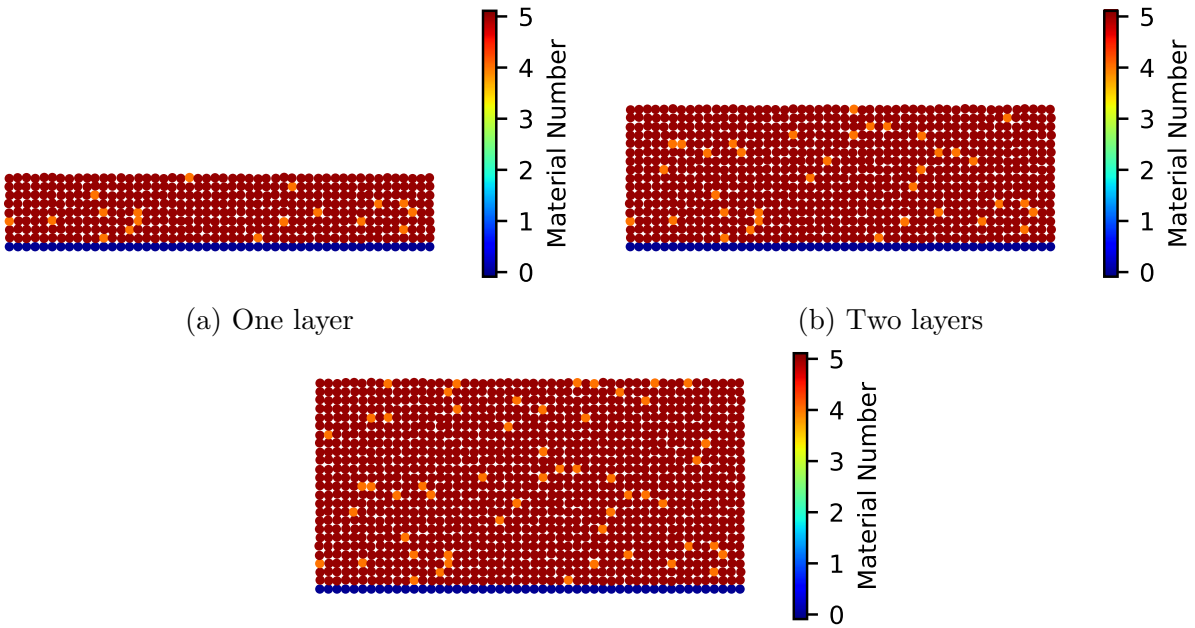

(a) One layer

(b) Two layers

(c) Three layers

Figure 5.8: Position of particles for studying the curing of multiple layers with a layer thickness of 16 µm. Each layer is introduced corresponding to the time necessary for the light to pass over the build domain twice, provided the light source scanning velocity for each test case in Table 5.4. Material numbers correspond to the wall, 0 or dark blue, photopolymer, 5 or red, and additive, 4 or orange.

5.3.2 Results

The results of the three layer curing study with a light source height of 3.2 cm and a scan velocity of 0.3 m/s are shown in Figure 5.9. With the exception of the initial configuration at time $t = 0$, the degree of cure shown is the last measured degree of cure prior to the addition of a new layer. In each of the figures each layer is still distinctly visible with different degrees of cure even though the monomer is permitted to diffuse through the domain. This is to be expected since the change in the monomer concentration due to diffusion is not considered in the degree of cure calculation. The diffusing monomer will impact the rate at which the material polymerizes, but since there exists a measureable discontinuity at the interface of the materials, the change in the rate is insufficient to make the degrees of cure smooth through the entire domain.

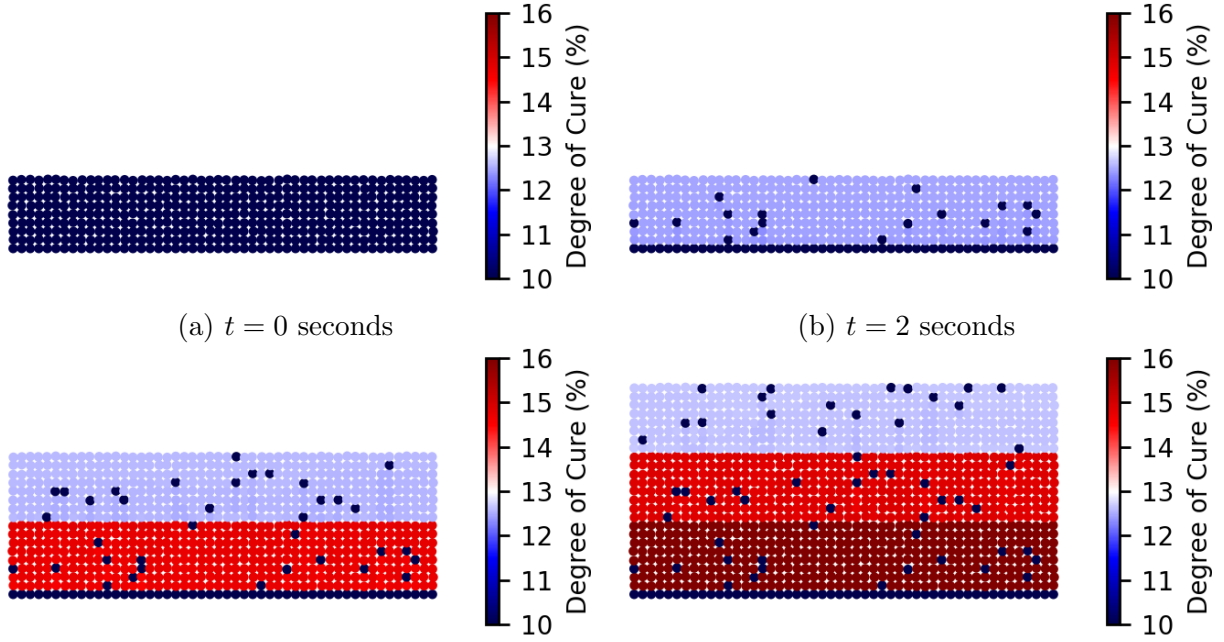

(a) $t = 0$ seconds

(b) $t = 2$ seconds

(c) $t = 4$ seconds

(d) $t = 6$ seconds

Figure 5.9: The degree of cure at four time steps starting at time $t = 0$ and ending at $t = 6$ seconds for test case 7 in Table 5.4.

The final degree of cure after three layers have been deposited and the light source has completed a total of six passes over the material for all nine test cases are shown in Figure 5.10. Looking across the columns of the figure in which the heights are fixed and the velocities change, the slower the light source the greater the degree of cure. This is expected since the slower light source provides more time for the reactions to occur and thus a greater degree of cure.

Looking down the rows of the figure in which the velocities are held fixed, the higher the light source the greater the degree of cure. While the intensity drops with increasing light source height, the increase in the height results in the material being exposed to the light source for a greater period of time and thus undergoing an active reaction for a greater portion of the printing process.

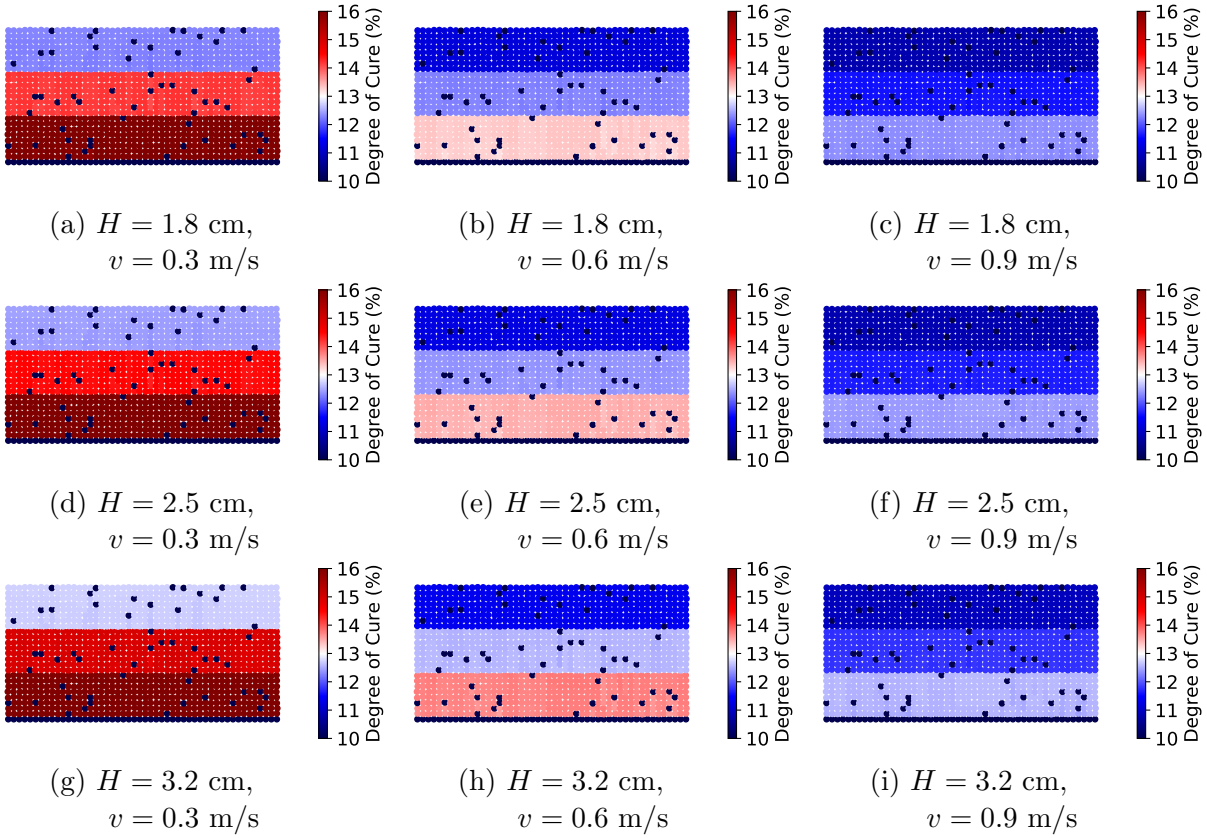

(a) $H = 1.8$ cm, $v = 0.3$ m/s (b) $H = 1.8$ cm, $v = 0.6$ m/s (c) $H = 1.8$ cm, $v = 0.9$ m/s

(d) $H = 2.5$ cm, $v = 0.3$ m/s (e) $H = 2.5$ cm, $v = 0.6$ m/s (f) $H = 2.5$ cm, $v = 0.9$ m/s

(g) $H = 3.2$ cm, $v = 0.3$ m/s (h) $H = 3.2$ cm, $v = 0.6$ m/s (i) $H = 3.2$ cm, $v = 0.9$ m/s

Figure 5.10: Final degree of cure profile for all nine test cases after six full passes of the light source.

To gain insight into the optimal process parameters, the maximum degree of cure on the top surface and the minimum degree of cure within the domain, and thus top layer, are considered. The minimum is considered since the objective is to have the entire layer to have reached a degree of cure greater than the gel point before the next layer is deposited. If no part of the layer has solidified, when the next layer is deposited, the droplet will impact into a liquid surface resulting in a splashing behavior and material spreading to an undesired location. If only the top half of the layer is solidified, the droplets of the next layer will no longer splash but the impact can lead to the still liquid resin being squeezed out of the specified domain near any edges.

The maximum degree of cure on the top surface is considered due to shrinkage that occurs during polymerization. The further a material proceeds past the gel point the larger the discontinuity between layers resulting in a greater difference in the shrinkage and thus larger internal stresses. The larger internal stresses increase the likelihood and severity of any curling or warpage that occurs.

The results of tracking the minimum and maximum degrees of cure in the top layer are shown in Figure 5.11. In all test cases, the degree of cure whether looking at the maximum or minimum increases with each layer deposited but the increase is small, roughly 0.1%. Since the increase is so small, it can be assumed that it is only necessary to consider a single layer to determine the optimal process parameters.

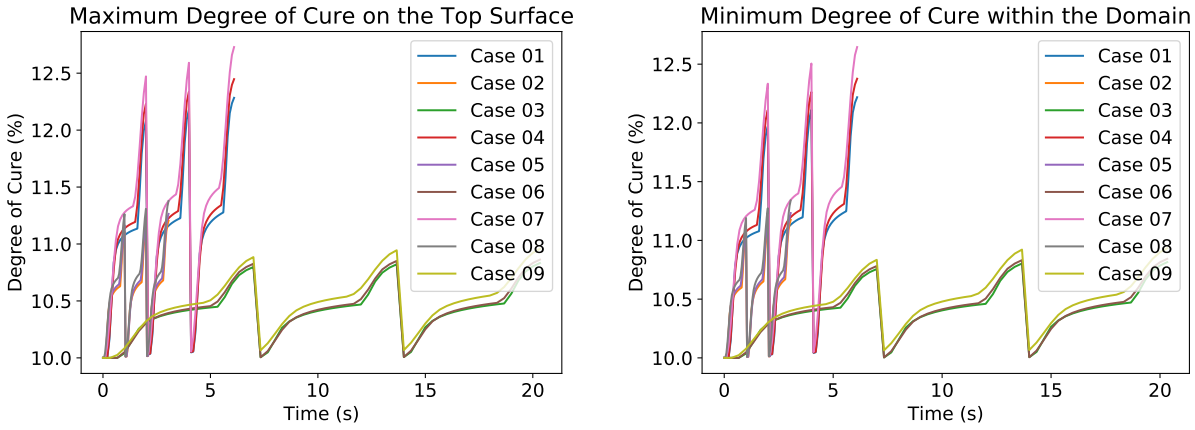

(a) (b)

Figure 5.11: (a) Maximum degree of cure on the top surface and (b) minimum degree of cure within the domain.

5.3.3 Objective Function Development

To develop an objective function, there are two options. The first is to use the minimum and maximum degrees of cure explicity where as the second uses the minimum and the difference between the minimum and maximum. Since the goal of the objective function is to identify printed results that have the smallest difference between two printed layers, the second option provides a better method for capturing this desired response. Specifically, the first places too much emphasis on the physical value of the maximum.

The general form of the objective function with measurable values of the maximum and minimum degree of cure in the top layer takes the form

$$\Pi = w_1 \left| \frac{C_{min}}{C^D_{min}} - 1 \right|^2 + w_2 \left| \frac{C_{max} - C_{min}}{C^D_{diff}} - 1 \right|^2 \tag{5.7}$$

where w_i is the weight for each term, C^D_{min} is the desired minimum degree of cure, and C^D_{diff} is the desired difference between the degrees of cure. The minimum desired degree of cure value is set to 18.0% to ensure that the entire layer has reached the gel point even if the optimal process parameters produce a final degree of cure less than the desired value. While ideally the degree of cure on the top and bottom of the layer are the same, the physics result in a gradient in the degree of cure. To account for the gradient the desired difference is set to be less than one percent of the desired minimum, 1.8%.

For the layer to be fully gelled, the minimum degree of cure should exceed the desired minimum value. This means that the weight must be greater when the current value is less than the desired, specifically, a value of 17% should results in a larger value in the objective function than 19%. To achieve this, the weight is doubled when the minimum is less than the desired value. Using the heaviside step function, the weight can be written as

$$w_1 = w_1 \left[H(C^D_{min} - C_{min}) + 1 \right] \tag{5.8}$$

where $H(x)$ is the heaviside step function. A similar process is applied to the difference in the degree of cure since a difference of 1% is better than 1.8% but rather than halving the weight, the weight is set to zero below the desired difference:

$$w_2 = w_2 H(C_{diff} - C^D_{diff}). \tag{5.9}$$

Finally, in the case both variables are above their desired value, the weights are set equal, that is

$$w_1 = w_2 = 0.5. \tag{5.10}$$

Plugging the parameters into the general objective function results in

$$\begin{aligned} \Pi =& 0.5 \left[H(18.0 - C_{min}) + 1 \right] \left| \frac{C_{min}}{18.0} - 1 \right|^2 \\ &+ 0.5 H(C_{diff} - 1.8) \left| \frac{C_{diff}}{1.8} - 1 \right|^2 \end{aligned} \tag{5.11}$$

To test the objective function for a wide range of degree of cure combinations, 100 random minimum and maximum degrees of cure are generated. First the minimum is generated by adding a random number between -5 and 5 to the desired minimum degree of cure. The maximum is then generated by multiplying the minimum by a random factor between 1 and 2. Results from applying the objective function to the randomly generated degrees of cure are shown in Figure 5.12.

Observe that as the maximum degree of cure increases, the objective function becomes larger and will always perform worse even when the minimum is near the desired value. Looking at the three best performing designs when the difference between the extreme values are small, the closer the minimum is to the desired minimum the better performing the design is. These observations indicate that the objective function is performing as desired.

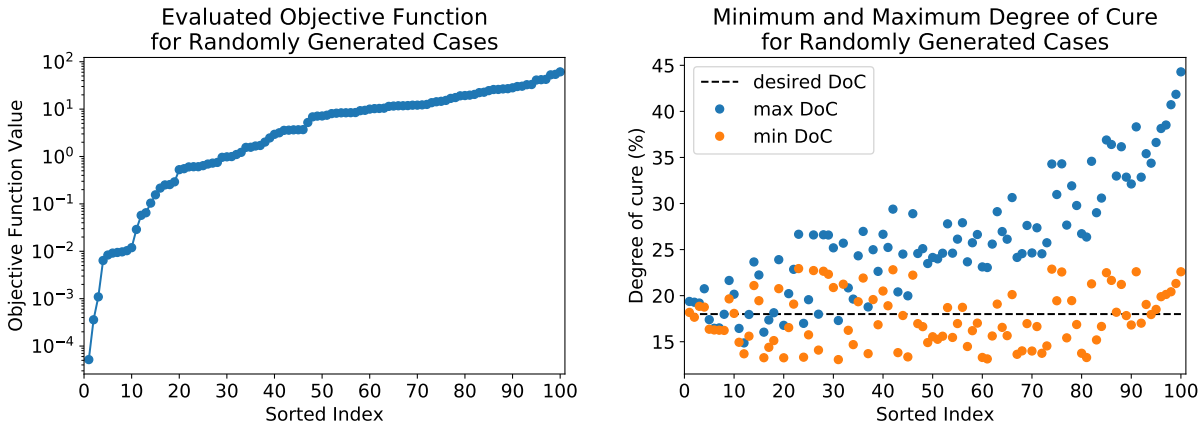

(a) (b)

Figure 5.12: The (a) evaluated objective function sorted from minimum to maximum value, best to worst performing, and (b) minimum and maximum degrees of cure of the sorted randomly generated test cases.

Applying the objective function to all nine test cases are shown in Figure 5.13. Using the output of the objective function, the test cases ordered from best performing to worst are, 7, 4, 1, 8, 5, 2, 9, 6, and 3. These results are expected based upon the plots of the minimum and maximum degrees of cure in Figure 5.11. Test cases 1, 4, and 7 get closest to the desired minimum as they are the only cases to exceed a degree of cure of 12%. Test case 7 performed the best achieving the greatest cure.

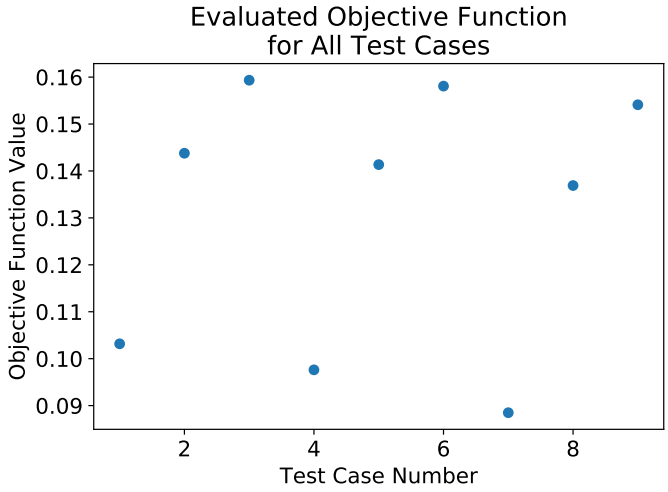

Figure 5.13: Objective function, Equation 5.11, evaluated at final time step for all nine test cases. Smaller values of the objective function correspond to better performance.

5.4 Conclusions

The two models demonstrated the importance of the design variables considered and the complex relationship between those variables during the inkjet printing process. From the layer formation simulations, it is observed that the surface profile shows a more observable sensitivity to the droplet spacing, or release frequency. On the other hand, the layer curing simulations demonstrate that the scan speed has a larger impact than the height of the light source on the final degree of cure.

To create the objective function, the observations made from visual inspection are converted into measureable values. For the layer formation simulations, the heights of the layer provided a better indicator of the print line quality than the width of the line. For the layered curing simulations, the minimum and the difference between the minimum and maximum in the top layer prodived the best insight into achieving the desired curing response. The new observations are then paired with the desired design values and weights are assigned to create the final objective function for each model. After testing the objective functions on randomly generated data, they are applied to the simulation results demonstrating their ability to capture the desired mechanical and curing response.

While useful to run the layer formation and curing separately in the development of the objective functions, to determine the optimal process parameters both processes must be performed in a single model problem. From the results shown in Figures 5.6 and 5.12, both functions are able to capture the desired response with an objective value on and order of 10^{-4} and thus the functions can be combined without requiring the weights be modified:

$$\begin{aligned}\Pi =& 1.0 \left| \frac{h_{avg}}{16.0} - 1 \right|^2 \\ &+ 0.5 H(h_{stdev} - 1.0) \left| \frac{h_{stdev}}{1.0} - 1 \right|^2 \\ &+ 0.5 H(h_{max} - h_{avg} - 1.0) \left| \frac{h_{max}}{h_{avg} + 1} - 1 \right|^2 \\ &+ 0.5 \left[H(18.0 - C_{min}) + 1 \right] \left| \frac{C_{min}}{18.0} - 1 \right|^2 \\ &+ 0.5 H(C_{diff} - 1.8) \left| \frac{C_{diff}}{1.8} - 1 \right|^2 .\end{aligned} \tag{5.12}$$

This new objective function can be utilized to obtain a set of process parameters that produce an optimal mechanical and curing response. Note that if desired, the weight for each term can be changed to accomodate a heavier preference on one variable or more variables.

Chapter 6

Summary and Future Work

6.1 Summary

This work introduced the photopolyermization process to the thermo-mechanical framework for the particle finite element method (PFEM) for the purpose of modeling the deposition and curing of the inkjet printing process. The specific goals of this work were to model the multiphysics reponse of an additive-photopolymer composite to understand the effects of additives and develop a characterization method that can be used to determine how well various inkjet printing process parameters performed.

The first model was the deposition of a single droplets onto a build surface with varying weight fractions of additives. It was observed that the shape of the final droplet varied depending on the weight fraction of additives, specifically the droplets tended to spread less as the weight fraction increased resulting in a smaller, taller final droplets. This impacts the layer formation process by requring the spacing between droplets being decreased to prevent gaps or thin regions from forming. While this can be addressed through the use of a roller, the additives are abrasives that damage the roller over time decreasing its ability to provide the desired level surface.

The next model was a SLA type system with varying weight fraction of additives for investigating the effects of additives on the degree of cure. The increase in weight fraction of additives results in a decrease in the degree of cure with greater effects deeper into the material. For the highest weight fractions the degree of cure on the top surface also decreased likely due to the additives preventing and limiting monomer diffusion. This translates into a slower propagation rate of the solidification front corresponding to the gel point.

These observations are important to note since the less the light can penetrate into the material the slower the internal portion of larger parts cures which can lead to under cured material. Additionally, the reduction in the solidification front translates into requiring longer periods of time for a new layer to fully gel. Allowing for the layer to cure for a longer periods of time can result in a greater difference in the degree of cure between layers and thus larger differences in the shrinkage leading to greater internal stresses.

With a basic understanding of how additives impact the thermo-mechano-chemical response of the material, the next model investigated the best method for characterizing the layer formation process through the deposition of four droplets onto a build surface. The most noticable observation was that the surface profile was sensitive to the droplet spacing. After converting the results into measureable values, it was observed that the average, maximum, and variation in the height of the final profile provided the most insight into how well the process parameters performed in producing smooth and stable print lines. Using these three measurable values, a single objective function capable of characterizing the profile into a single value was developed.

The objective function was first tested on a set of randomly generated profiles and shown to capture the desired surface characteristics. Next, the objective function was applied to the models and shown to predict the same best and worst performing process parameters as those determined through visual inspection. A noteable observation was that the lower tested ejection velocity, 5 m/s, always outperformed the higher ejection velocity, 8 m/s. This informs us that the range of possible ejection velocities can be narrowed during an optimization process.

The model was the curing of multiple layers. From the final cure profiles, it is was demonstrated that the scan speed of the light source had a larger impact than the height on the final degree of cure. In order to develop an objective function, it was noticed that the individual layers were still distinguishable, this allowed for the measureable values to come from a single layer, specifically the maximum and minimum degree of cure within the top most layer. These two values were selected as they are able to ensure the entire layer solidifies past the gel point while also minimizing the difference in the degree of cure between layers. These two measurable values were then converted into a single objective function capable of characterizing the curing profiles into a single value.

Testing the objective function on randomly generated sets of minimums and maximums demonstrated that the objective function narrowed in on curing profiles with small variations between the extreme values and had minimum degrees of cure close to the desired. Applying the objective function to the models provided minimal insight since the maximum degree of cure in all cases was below the desired minimum degree of cure. The only current conclusions that can be drawn are that a scan speed of 0.3 m/s is too fast or a second light source leading the print heads may be required.

Finally, combining both objective functions provides a method for characterizing how well the process parameters are able to produce print lines for nanoparticle-polymeric composites for use in inkjet printing.

6.2 Future Work

The work presented here is limited to two-dimensional problems with the mechanical and curing models run separately for computational efficiency. To allow for more complex models, the algorithm presented in this work should be modified for parallelization. This will allow for the larger domains containing more particles required by a full three-dimensional representation.

Increased computational efficiency also benefits the two-dimensional problems as it allows for the modeling of a full system in which a layer is deposited then cured. By combining the mechanical and curing models, the final objective function developed in this work can be utilized for process parameter optimization. This is best illustrated by the genetic algorithm in which random sets of process parameters are generated then evaluated until optimal parameters are found. Each set requires running the PFEM algorithm once so the faster a simulation solution is generated, the faster the genetic algorthim can find the optimal parameters.

A final benefit is that the work can be extended to include more of the overall inkjet printing process. The model can be extended to include the droplet formation from the moment of ejection from the nozzle to the motion through the ambient environment.

Another limitations of this work is that the viscosity model is limited by the experimental data available. Work to improve the viscosity model to include the degree of cure would allow this work to be expanded to modeling of a more comprehensive layering study. The updating of the viscosity is required since the current viscosity model results in the material staying fluid even as it passes the gel point, or the point at which is can retain its shape. This means that the work as is cannot model the full layer upon layer deposition then curing process.

Updating the viscosity model is a quick update as many simple models exist, the challenge is that they require constant parameters fit to experimental data that does not currently exist. One such model was presented by Castro and Macosko [5]

$$\frac{\mu}{\mu_0} = \left(\frac{C_g}{C_g - C}\right)^{c_1 + c_2 C} \tag{6.1}$$

where C_g is the degree of cure at the gel point, C is the current degree of cure, and c_1 and c_2 are constants determined from fitting to experimental data.

Finally, the PFEM framework with photopolymerization is not limited to the inkjet printing processess with photopolymers. Extensive prior work has gone into studying and developing tools to predict the print profile of a domain with sterolithography, but they all depend only on the curing response. Inclusion of the motion of the fluid has the potential to increase the accuracy of the predicted results. Additionally, if the material properties are set accordingly, the curing response can be removed and the inclusion of a light source allows for this frame work to be applicable to other additive manufacturing processes such as selective laser sintering.

Bibliography

[1] B. Abedian and M. Kachanov. "On the effective viscosity of suspensions". In: *International Journal of Engineering Science* 48.11 (2010), pp. 962–965.

[2] Dimitris S. Achilias and Panoraia I. Siafaka. "Polymerization kinetics of poly(2-hydroxyethyl methacrylate) hydrogels and nanocomposite materials". In: *Processes* 5.2 (2017), p. 21.

[3] Paulo Jorgeda Silva Bártolo. "Theoretical and modeling aspects of curing reactions". In: *Stereolithography*. Ed. by Paulo Jorge Bártolo. Springer, 2011, pp. 209–241.

[4] M. de Berg et al. *Computational geometry: Algorithms and applications*. Verlag Berlin Heidelberg: Springer, 2008.

[5] J. M. Castro and C. W. Macosko. "Studies of mold filling and curing in the reaction injection molding process". In: *AIChE Journal* 28.2 (1982), pp. 250–260.

[6] A. Chiolerio, I. Roppolo, and M. Sangermano. "Radical diffusion engineering: tailored nanocomposite materials for piezoresistive inkjet printed strain measurement". In: *Composites Science and Technology* 72.12 (2013), pp. 1387–1395.

[7] K. Chizari et al. "Three-dimensional printing of highly conductive polymer nanocomposites for EMI shielding applications". In: *Materials Today Communications* 11 (2017), pp. 112–118.

[8] Alexandre Joel Chorin. "Numerical solution of the Navier-Stokes equations". In: *Mathematics of computation* 22.104 (1968), pp. 745–762.

[9] Alexandre Joel Chorin and Jerrold E. Marsden. *A mathematical introduction to fluid mechanics*. Vol. 3. New York: Springer, 1993.

[10] B. Derby and N. Reis. "Inkjet printing of highly loaded particulate suspensions". In: *MRS bulletin* 28.11 (2003), pp. 815–818.

[11] Brian Derby. "Inkjet printing of functional and structural materials: fluid property requirements, feature stability, and resolution". In: *Annual Review of Materials Research* 40 (2010), pp. 395–414.

[12] P.C. Duineveld et al. "Ink-jet printing of polymer light-emitting devices". In: *Organic Light-Emitting Materials and Devices V* 4464 (2002), pp. 59–68.

[13] H. Edelsbrunner and E. P. Mucke. "Three-dimensional alpha shapes". In: *ACM Transactions on Graphics (TOG)* 13.1 (1994), pp. 43–72.

[14] A. Einstein. "A new determination of molecular dimensions". In: *Annals of Physics* 19.34 (1911), 591592.

[15] Amelia Elliott. "The effects of quantum dot nanoparticles on the polyjet direct 3D printing process". PhD dissertation. Virginia Polytechnic Institute and State University, 2014.

[16] Amelia M. Elliott et al. "An investigation of the effects of quantum dot nanoparticles on photopolymer resin for use in polyjet direct 3D printing". In: *2012 SFF SSymposium*. 2012.

[17] Amelia M. Elliott et al. "Inkjet printing of quantum dots in photopolymer for use in additive manufacturing of nanocomposites". In: *Advanced Engineering Materials* 15.10 (2013), pp. 903–907.

[18] R. D. Farahani, M. Dube, and D. Therriault. "Three-dimensional printing of multifunctional nanocomposites: manufacturing techniques and applications". In: *Advanced Materials* 28.28 (2016), pp. 5794–5821.

[19] R. D. Farahani et al. "Reinforcing epoxy nanocomposites with functionalized carbon nanotubes via biotinstreptavidin interactions". In: *Composites Science and Technology* 72 (2012), 13871395.

[20] Lawrance Flach and Richard P. Chartoff. "A process model for nonisothermal photopolymerization with a laser light source. I: Basic model development". In: *Polymer Engineering and Science* 35.6 (1995), pp. 483–492.

[21] Lawrance Flach and Richard P. Chartoff. "A process model for nonisothermal photopolymerization with a laser light source. II: Behavior in the vicinity of a moving exposed region". In: *Polymer Engineering and Science* 35.6 (1995), pp. 493–498.

[22] Ian Gibson, David Rosen, and Brent Stucker. *Additive Manufacturing Technologies: 3D Printing, Rapid Prototyping, and Direct Digital Manufacturing*. New York: Springer, 2014.

[23] M. D. Goodner and C. N. Bowman. "Development of a comprehensive free radical photopolymerization model incorporating heat and mass transfer effects in thick films". In: *Chemical Engineering Science* 57.5 (2002), pp. 887–900.

[24] M. D. Goodner and C. N. Bowman. "Modeling primary radical termination and its effects on autoacceleration in photopolymerization kinetics". In: *Macromolecules* 32.20 (1999), pp. 6552–6559.

[25] M. D. Goodner, H. R. Lee, and C. N. Bowman. "Method for determining the kinetic parameters in diffusion-controlled free-radical homopolymerizations". In: *Industrial and engineering chemistry research* 36.4 (1997), pp. 1247–1252.

[26] S. R. Idelsohn, Limache A. Marti J., and E. Oñate. "Unified Lagrangian formulation for elastic solids and incompressible fluids: application to fluid-structure interaction problems via the PFEM". In: *Computer Methods in Applied Mechanics and Engineering* 197.19 (2008), pp. 1762–1776.

[27] S. R. Idelsohn, E. Oñate, and F. D. Pin. "The particle finite element method: a powerful tool to solve incompressible flows with freesurfaces and breaking waves". In: *International journal for numerical methods in engineering* 61.7 (2004), pp. 964–989.

[28] S. R. Idelsohn et al. "Fluidstructure interaction using the particle finite element method". In: *Computer methods in applied mechanics and engineering* 195.17-18 (2006), pp. 2100–2123.

[29] S. R. Idelsohn et al. "The particle finite element method for multi-fluid flows". In: *Particle-Based Methods*.

[30] O. Ivanova, C. Williams, and T. Campbell. "Additive manufacturing (AM) and nanotechnology: promises and challenges". In: *Rapid Prototyping Journal* 19.5 (2013), pp. 353–364.

[31] A. A. Khalate et al. "Performance improvement of a drop-on-demand inkjet printhead using an optimization-based feedforward control method". In: *Control Engineering Practice* 19.8 (2011), pp. 771–781.

[32] L. L. Lebel et al. "Ultraviolet-assisted direct-write fabrication of carbon nanotube/polymer nanocomposite microcoils". In: *Advanced Materials* 22.5 (2010), pp. 592–596.

[33] S.J. Leigha et al. "A miniature flow sensor fabricated by micro-stereolithography employing a magnetite/acrylic nanocomposite resin". In: *Sensors and Actuators A: Physical* 168.1 (2011), pp. 66–71.

[34] Jin Hong Lim et al. "Selective deposition modeling using cw uv led curing". Pat. US 8,876,513 B2. 2014.

[35] Agnieszka Marcinkowska, Dawid Przadka, and Ewa Andrzejewska. "Modification of poly-HEMA with nonreactive POSS derivatives by in situ photopolymerization". In: *Journal of Thermal Analysis and Calorimetry* (2019), pp. 1–15.

[36] A. V. Markov. "Rheological behavior of high filled polymers. Influence of fillers". In: *Materialwissenschaft und Werkstofftechnik: Entwicklung, Fertigung, Prfung, Eigenschaften und Anwendungen technischer Werkstoffe* 39.3 (2008), pp. 227–233.

[37] M. Mier-Torrecilla, S. R. Idelson, and E. Oñate. "Advances in the simulation of multifluid flows with the particle finite element method. Application to bubble dynamics". In: *International Journal for Numerical Methods in Fluids* 67.11 (2011), pp. 1516–1539.

[38] Sneha Mohan et al. "Rheology and Processing of Inorganic Nanomaterials and Quantum Dots/Polymer Nanocomposites". In: *Rheology and Processing of Polymer Nanocomposites*.

[39] George Odian. *Principles of polymerization*. New Jersey: John Wiley & Sons, 2004.

[40] Tim Osswald and Natalie Rudolph. *Polymer rheology: Fundamentals and applications*. Cincinnati: Hanser Publishers, 2015.

[41] E. Oñate, A. Franci, and J. M. Carbonell. "A particle finite element method (pfem) for coupled thermal analysis of quasi and fully incompressible flows and fluid-structure interaction problems". In: *Numerical Simulations of Coupled Problems in Engineering*.

[42] E. Oñate et al. "Analysis of the melting, burning and flame spread of polymers with the particle finite element method". In: *Computer Assisted Methods in Engineering and Science* 20.3 (2013), 165184.

[43] E Oñate et al. "Melting and spread of polymers in fire with the particle finite element method". In: *International Journal for Numerical Methods in Engineering* 81.8 (2010), pp. 1046–1072.

[44] Matthias Sabel et al. "Application of the particle finite element method in machining simulation discussion of the alpha-shape method in the context of strength of materials". In: *Journal of Computational and Informational Science in Engineering* 17.1 (2017), pp. 011002–1 –011002–7.

[45] Benay Sager and David W. Rosen. "Simulation methods for stereolithography". In: *Stereolithography*. Ed. by Paulo Jorge Bártolo. Springer, 2011, pp. 183–207.

[46] Kris Alan Schmidt. "Selective deposition modeling with curable phase change materials". Pat. US 6,841,116 B2. 2005.

[47] Kris Alan Schmidt et al. "Ultra-violet light curable hot melt composition". Pat. US 6,841,589 B2. 2005.

[48] Andreas Schmocker et al. "Multi-scale modeling of photopolymerization for medical hydrogel-implant design". In: *Biomedical Applications of Light Scattering VII*. Vol. 8592. International Society for Optics and Photonics. 2013, p. 85921D.

[49] Jaroslaw Siedlecki and Mariusz Ciesielski. "Mathematical model for thermal processes in photopolymerization". In: *Scientific Research of the Institute of Mathematics and Computer Science* 11.4 (2012), pp. 113–119.

[50] M. Singh et al. "Inkjet PrintingProcess and Its Applications". In: *Advanced Materials* 22.6 (2010), pp. 673–685.

[51] Dan Soltman and Vivek Subramanian. "Inkjet-printed line morphologies and temperature control of the coffee ring effect". In: *Langmuir* 24.5 (2008), pp. 2224–2231.

[52] C.D. Stow and M.G. Hadfield. "An experimental investigation of fluid flow resulting from the impact of a water drop with an unyielding dry surface". In: *Proceedings of the Royal Society of London. A. Mathematical and Physical Sciences* 373.1755 (1981), pp. 419–441.

[53] Stratasys. *Stratasys J735 and J750*. `https://www.stratasys.com/3d-printers/j735-j750`. 2019.

[54] J. Stringer and B. Derby. "Formation and Stability of Lines Produced by Inkjet Printing". In: *Langmuir* 26.12 (2010), pp. 10365–10372.

[55] 3D Systems. *MultiJet Plastic Printers*. `https://www.3dsystems.com/sites/default/files/2018-11/3d-systems-mjp-2500-tech-specs-usen-2018-11-05-web.pdf`. 2018.

[56] K. David Wegner and Niko Hildebrandt. "Quantum dots: bright and versatile in vitro and in vivo fluorescence imaging biosensors". In: *Chemical Society Reviews* 44.14 (2015), pp. 4792–4834.

[57] J.D. Yu, S. Sakai, and J.A. Sethian. "A coupled level set projection method applied to ink jet simulation". In: *Interfaces and Free Boundaries* 5.4 (2003), pp. 459–482.

[58] J.D. Yu, S. Sakai, and J.A. Sethian. "A coupled quadrilateral grid level set projection method applied to ink jet simulation". In: *Journal of Computational Physics* 206.1 (2005), pp. 227–251.

[59] J.D. Yu, S. Sakai, and J.A. Sethian. "Two-phase viscoelastic jetting". In: *Journal of Computational Physics* 220.2 (2007), pp. 568–585.

[60] Chuanxin Zhai et al. "One-pot synthesis of biocompatible CdSe/CdS quantum dots and their applications as fluorescent biological labels". In: *Nanoscale Res Lett* 6.1 (2011), p. 31.